

The Ring Nebula Around the Blue Supergiant SBW1: Pre-Explosion Snapshot of a SN 1987A Twin^{*†}

Nathan Smith^{1‡}, W. David Arnett¹, John Bally², Adam Ginsburg² & Alexei V. Filippenko³

¹*Steward Observatory, 933 N. Cherry Ave., Tucson, AZ 85721, USA*

²*Center for Astrophysics and Space Astronomy, Campus Box 389, University of Colorado, Boulder, CO 80309, USA*

³*Department of Astronomy, University of California, Berkeley, CA 94720-3411, USA*

Accepted 2012 Nov 14, Received 2012 Oct 17, in original form 2012 Oct 17

ABSTRACT

SBW1 is a B-type supergiant surrounded by a ring nebula that is a nearby twin of SN 1987A’s progenitor and its circumstellar ring. We present images and spectra of SBW1 obtained with the *Hubble Space Telescope* (*HST*), the *Spitzer Space Telescope*, and Gemini South. *HST* images of SBW1 do not exhibit long Rayleigh-Taylor (R-T) fingers, which are presumed to cause the “hotspots” in the SN 1987A ring when impacted by the blast wave, but instead show a geometrically thin ($\Delta R/R \lesssim 0.05$) clumpy ring. The radial mass distribution and size scales of inhomogeneities in SBW1’s ring closely resemble those in the SN 1987A ring, but the more complete disk expected to reside at the base of the R-T fingers is absent in SBW1. This structure may explain why portions of the SN 1987A ring between the hotspots have not yet brightened, more than 15 years after the first hotspots appeared. The model we suggest does not require a fast wind colliding with a previous red supergiant wind, because a slowly expanding equatorial ring may be ejected by a rotating blue supergiant star or in a close binary system. More surprisingly, high-resolution images of SBW1 also reveal diffuse emission filling the interior of the ring seen in $H\alpha$ and in thermal-infrared (IR) emission; ~ 190 K dust dominates the 8–20 μm luminosity (but contains only $10^{-5} M_{\odot}$ of dust). Cooler (~ 85 K) dust resides in the equatorial ring itself (and has a dust mass of at least $5 \times 10^{-3} M_{\odot}$). Diffuse emission extends inward to $\sim 1''$ from the central star, where a paucity of $H\alpha$ and IR emission suggests an inner hole excavated by the B-supergiant wind. We propose that diffuse emission inside the ring arises from an ionised flow of material photoevaporated from the dense ring, and its pressure prevents the B-supergiant wind from advancing in the equatorial plane. This inner emission could correspond to a structure hypothesised to reside around Sk–69°202 that was never directly detected. If this interpretation is correct, it would suggest that photoionisation can play an important dynamical role in shaping the ring nebula, and we speculate that this might help explain the origin of the polar rings around SN 1987A. In effect, the photoevaporative flow shields the outer bipolar nebula at low latitudes, whereas the blue-supergiant wind expands freely out the poles and clears away the polar caps of the nebula; the polar rings reside at the intersection of these two zones.

Key words: binaries: general — circumstellar matter — stars: evolution — stars: mass loss — stars: winds, outflows — supernovae: general — supernovae: individual (SN 1987A)

* Based in part on observations made with the NASA/ESA *Hubble Space Telescope*, obtained at the Space Telescope Science Institute, which is operated by the Association of Universities

for Research in Astronomy, Inc. (AURA), under NASA contract NAS5-26555.

† Based in part on observations obtained at the Gemini Observatory, which is operated by AURA, under a cooperative agreement

1 INTRODUCTION

SN 1987A in the Large Magellanic Cloud (LMC) is one of those vexing examples of Murphy’s law, where the nearest and best-studied supernova (SN) in modern times also appears unique when compared to the population of known extragalactic core-collapse supernovae (SNe). It is an odd-ball, consisting of a peculiar SN type having a slow rise to peak, attributed to the relatively compact nature of its (also unusual and unexpected) blue-supergiant (BSG) progenitor (Arnett 1987, 1989; Arnett et al. 1989). SN 1987A is the only SN near enough to obtain a clear picture of its spatially resolved circumstellar nebula, but its bizarre triple-ring nebula still defies adequate explanation (Luo & McCray 1991; Blondin & Lundqvist 1993; Martin & Arnett 1995; Collins et al. 1999; Morris & Podsiadlowski 2009), and does not conform to the hourglass structures commonly seen in bipolar planetary nebulae and bipolar nebulae around massive stars.

There are, however, a few objects known that appear similar to SN 1987A in that they have prominent equatorial ring nebulae with bipolar lobes or rings surrounding BSG central stars. In this paper, we present a detailed study of the recently discovered ring nebula SBW1 (Smith et al. 2007). Two other known bipolar ring nebulae around massive stars are HD 168625 and Sher 25, which are discussed in detail elsewhere (Smith 2007; Brandner et al. 1997). Of these three, SBW1 appears to most closely resemble the nebula around SN 1987A and the physical parameters of its progenitor star.

Before massive stars explode as SNe, they can shed considerable mass as they attempt to remove their outer H-rich envelope. If they fail to shed their H envelopes, they will typically remain as red supergiants (RSGs) and will die as SNe of Type II. One expects single stars in the lower initial mass ranges of core-collapse SNe (8–20 M_{\odot}) to retain their H envelopes and explode as RSGs, and this expectation is largely confirmed by pre-explosion detections of progenitor stars of SNe II-P (e.g., Smartt 2009; Leonard 2011, and references therein). SN 1987A challenged our view of stellar evolution because it was a SN II from an explosion of a BSG, not a RSG, with an initial mass of 18–20 M_{\odot} (see Arnett et al. 1989, and references therein). The reason that the progenitor was a BSG is still unclear, but various scenarios involving close binary evolution, binary mergers, rapid rotation, and enhanced mass loss have been suggested.

Pre-explosion data for SN1987A’s progenitor star Sk–69°202 establish that it appeared to be a fairly normal B3 I supergiant (Walborn et al. 1989; Rousseau et al. 1978). Therefore, our conjectures about the progenitor and its pre-SN mass loss depend heavily on studies of the remarkable ring nebula surrounding the SN, made famous in early *Hubble Space Telescope* (*HST*) images (e.g., Plait et al. 1995; Burrows et al. 1995). Kinematic studies of the nebula’s expansion indicate that it was ejected by the progenitor star roughly 10^4 yr before exploding as a SN (Meaburn et al.

with the National Science Foundation (NSF) on behalf of the Gemini partnership, which comprises the NSF (US), the Particle Physics and Astronomy Research Council (UK), the National Research Council (Canada), CONICYT (Chile), the Australian Research Council (Australia), CNPq (Brazil), and CONICET (Argentina).

‡ Email: nathans@as.arizona.edu

Table 1. New Observations of SBW1

UT Date	Tel./Instr.	Filter	Exp.
2009 Dec. 08	<i>HST</i> /WFC3	F502N	2×210 s
2009 Dec. 08	<i>HST</i> /WFC3	F656N	4×210 s
2009 Dec. 08	<i>HST</i> /WFC3	F658N	4×240 s
2010 May 18	<i>HST</i> /STIS	G750M/6581	2×2070 s
2010 Mar. 29	Gemini South/T-ReCS	8.8 μm	4×1570 s
2008 Mar. 30	Gemini South/T-ReCS	11.7 μm	4×600 s
2009 Jun. 09	Gemini South/T-ReCS	11.7 μm	4×1577 s
2009 Apr. 18	Gemini South/T-ReCS	18 μm	2×2065 s

1995; Crotts & Heathcote 2000). The ejection and shaping mechanisms of this nebula are intimately linked to the star’s peculiar evolution just before explosion, but our understanding of that process is still tenuous. The poor understanding of how the ring nebula formed has become a more pressing problem in recent years. We are now lucky enough to witness a spectacular collision as the blast wave of the SN overtakes the ring nebula ejected by the progenitor, predicted shortly after the discovery of the nebula (Luo & McCray 1991).

The SN 1987A blast wave first began to collide with the dense circumstellar ring in 1997, heralded by the appearance of new “hot spots” in the ring (Sonneborn et al. 1998; Michael et al. 1998, 1999). These hotspots had broader line widths than the rest of the ring, confirming that they were bright because a shock was being driven into the dense clumps. These clumps were thought to be the ends of long “fingers” created by Rayleigh-Taylor (R-T) instabilities at the contact discontinuity between the slow RSG wind and the fast BSG wind. Since the hotspots first appeared in 1997, many more spots have brightened all around the ring (Sugerman et al. 2002), although the hotspots have not yet merged into a contiguous bright ring as one might expect when the blast wave catches up to gas in between the R-T fingers.

In the decade between explosion and the start of this collision with the ring, the blast wave was expanding through the relatively low-density region interior to the ring. Radio emission and hydrodynamic models suggest that the BSG wind had a surprisingly low mass-loss rate of $\sim 10^{-7} M_{\odot} \text{ yr}^{-1}$ (Stavely-Smith et al. 1993; Blondin & Lundqvist 1993; Martin & Arnett 1995; Chevalier & Dwarkadas 1995). The expansion rate of the blast wave through this low-density progenitor wind was fast at first, but then slowed (Gaensler et al. 2000), attributed to the shock running into a higher-density H II region caused by photoionised material from the dense RSG wind (Chevalier & Dwarkadas 1995; Meyer 1997). While the existence of this H II region can account for some observed characteristics of the blast-wave expansion, emission from this feature itself was not directly observed before it was hit by the blast wave. One of the key results from our analysis below is that such a feature is seen directly in the similar nebula around SBW1.

A different approach to shed light on the pre-SN evolution of SN 1987A is to study nearby analogs of SN 1987A’s progenitor that have not yet exploded. As noted above, three possible cousins of SN 1987A’s progenitor are known: Sher 25, HD 168625, and SBW1. Of these, SBW1 appears the most similar in terms of the nebular structure and the luminosity of the central star, but it is not as extensively studied as the other two. Smith et al. (2007) first discovered

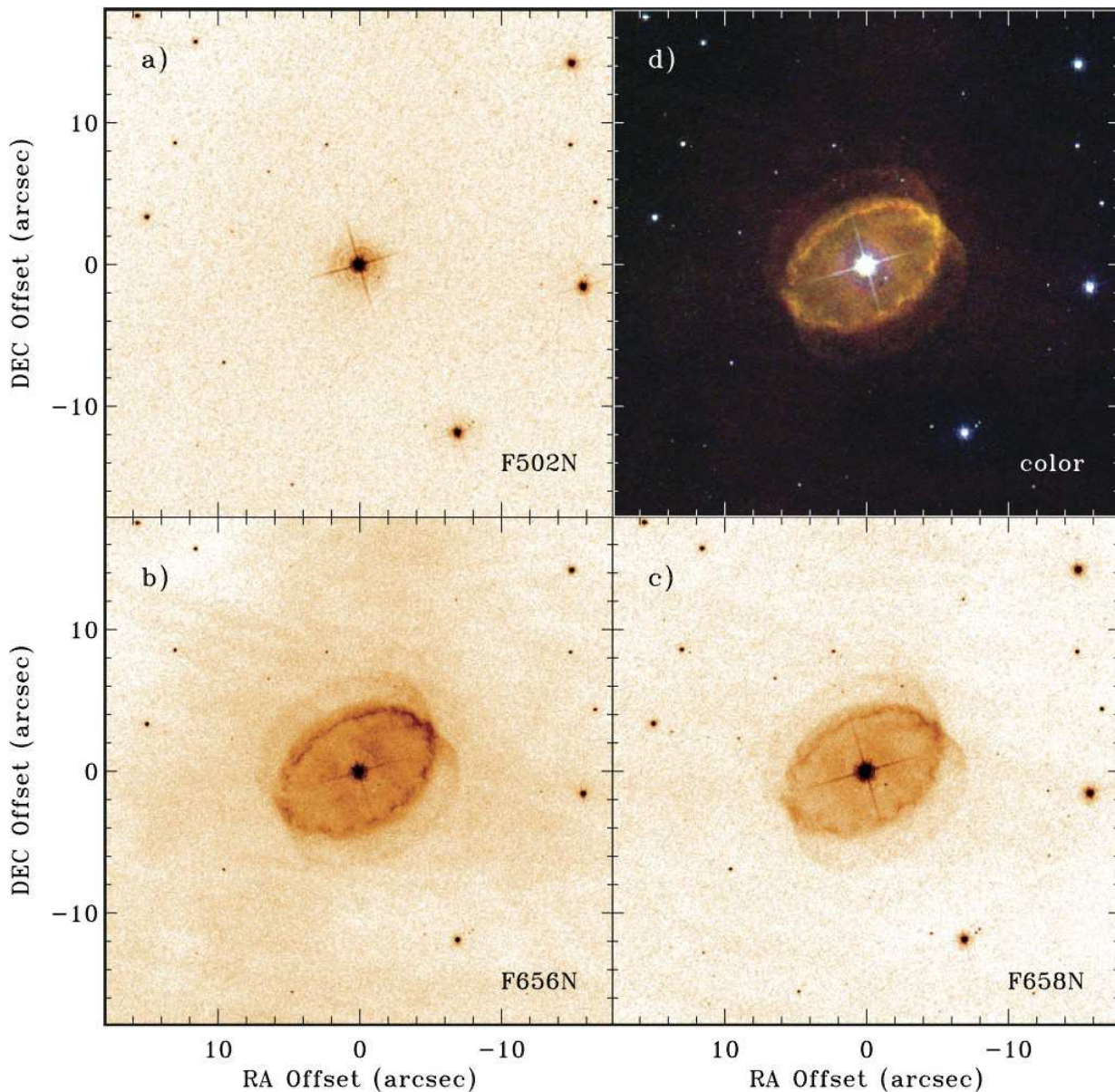


Figure 1. The new *HST*/WFC3 images of SBW1. Panels (a), (b), and (c) are taken in the F502N [O III] λ 5007, F656N H α , and F658N [N II] λ 6584 filters, respectively, displayed in false colour. Panel (d) is a colour composite of the three *HST*/WFC3 images, with F502N in blue, F658N in green, and F656N in red. The origin is at the position of the star, at $\alpha_{J2000} = 10^h 40^m 18^s.60$, $\delta_{J2000} = -59^\circ 49' 12''.5$.

SBW1 and performed the initial study of its nebula. While it is seen projected in the Carina Nebula star-forming region, its positive radial velocity suggests that it is actually located at a much larger distance *behind* the Carina Nebula; a distance of ~ 7 kpc rather than the well-established 2.3 kpc distance to Carina (Smith 2006) also provides a better match between the expected luminosity from the B1.5 Iab spectral type and the observed magnitude and relatively low reddening. This distance makes the luminosity of SBW1 comparable to that of Sk-69 $^{\circ}$ 202, suitable for an 18–25 M_{\odot} progenitor star. From our more detailed analysis below, we find that SBW1 is indeed a virtual twin of the progenitor of SN 1987A and its circumstellar environment.

2 OBSERVATIONS

2.1 HST/WFC3 Images

Following discovery in our ground-based observations (Smith et al. 2007), we imaged SBW1 using the newly installed WFC3 camera onboard *HST* on 2009 Dec. 8. (UT dates are used throughout this paper; see Table 1.) We used three filters: F502N sampling [O III] λ 5007, F656N sampling H α , and F658N sampling [N II] λ 6584. We employed standard image-reduction techniques, and the resulting monochromatic F502N, F656N, and F658N images are shown in Figures 1a, 1b, and 1c, respectively, whereas a colour composite of the three is shown in Figure 1d.

The *HST*/WFC3 images detect no [O III] emission from the ring nebula itself. This suggests that there is no nearby

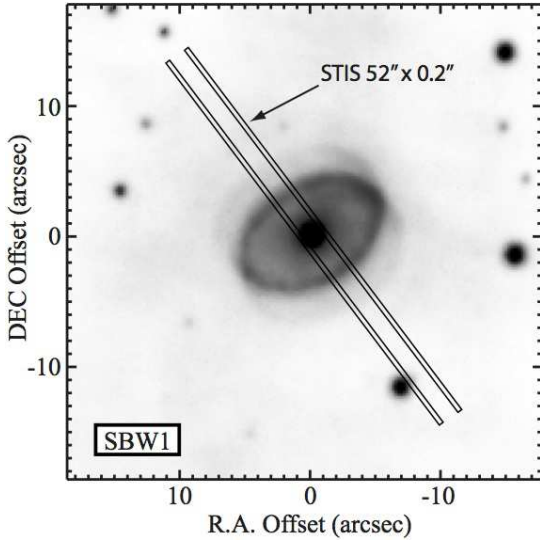


Figure 2. Positions of the two STIS long-slit apertures superposed on the ground-based $H\alpha$ image of SBW1 from Smith et al. (2007). The fluxes at these two positions were added to produce the two-dimensional spectrum shown in Figure 3.

source of hard-ultraviolet (UV) photons (> 35 eV) that can ionise O^+ to O^{++} in the circumstellar gas. There are apparently plenty of hard ionising photons from the much more massive early O-type stars in proximate regions of the Carina Nebula (also evidenced by the bright diffuse $[O\ III]$ emission seen around SBW1), so this provides yet another argument that SBW1 is not actually located within the Carina Nebula, but is instead far *behind* it and seen in projection (Smith et al. 2007). Similarly, we detect no features in absorption associated with the circumstellar dust in SBW1, contrary to expectations for dust features in silhouette against a background screen of an H II region.

The $H\alpha$ and $[N\ II]$ images reveal emission structures that are essentially identical. In a F656N – F658N difference image (not shown), the nebula vanishes almost completely, except for a small wisp of emission in the diffuse inner part of the ring at the 1% level, which could easily be attributable to some foreground absorption or emission in the Carina Nebula. As we will see below, our analysis of the continuum-subtracted emission in *HST* Space Telescope Imaging Spectrograph (STIS) spectra shows no variation in the $H\alpha/[N\ II]$ flux ratio across the ring, consistent with flux ratios measured in images (STIS spectra are preferred for this comparison, since scattered starlight can be subtracted). Thus, the gas in the dense and thin equatorial ring, the gas in the outer bipolar regions, and the more diffuse gas filling the interior of the ring are likely to all have the same relative N/H abundance. This is important for some models of the formation of the nebula (see below).

The most interesting results of the *HST* imaging are (1) the detailed structure in the equatorial ring itself, seen at roughly 7 times the effective *spatial* resolution (not angular resolution) provided by *HST* images of the more distant SN 1987A ring, and (2) diffuse emission structures inside the ring, which are associated with hot dust features (see below). Both of these provide important clues about the structure and origin of the nebula into which the SN 1987A

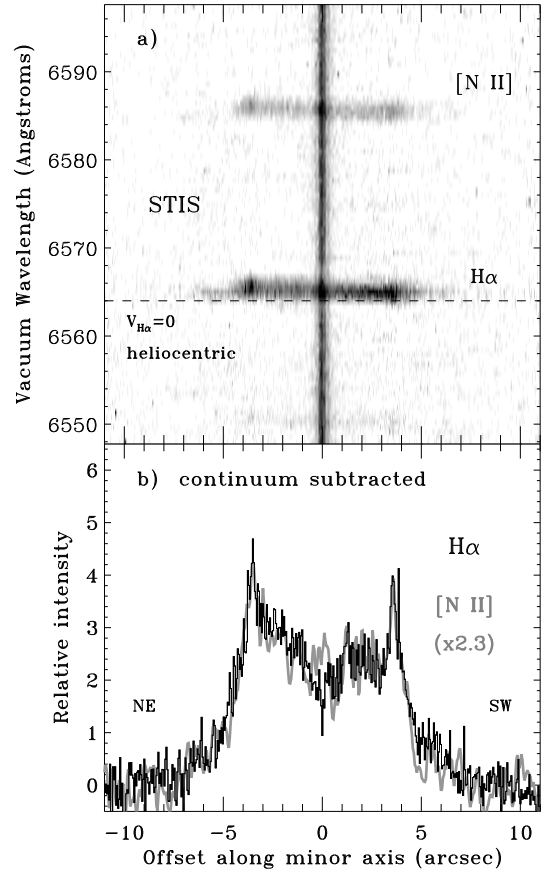


Figure 3. Panel (a) shows the two-dimensional STIS spectrum of the SBW1 ring centred on $H\alpha$ and $[N\ II]\ \lambda 6584$, corresponding to the sum of the fluxes in the two slits shown in Figure 2. Panel (b) shows a tracing of the continuum-subtracted flux of both $H\alpha$ (black) and $[N\ II]$ (grey) along the slit. Positional offset along the slit is shown on the horizontal axis in both panels, with northeast (NE) oriented to the left. From the difference in Doppler shift along the slit, it is clear that the NE side is the receding side of the equatorial ring.

blast wave has been expanding. The specific structures and implications are discussed in §3 and §4.

2.2 *HST*/STIS Spectra

The SBW1 ring was also observed with *HST*/STIS on 2010 May 18 (UT, see Table 1). The $52'' \times 0.2''$ slit aperture was oriented along position angle $+37^\circ$, at two offset positions on either side of the central star as shown in Figure 2.

Figure 3a indicates that there is a slight velocity gradient across the ring, such that the NE side of the equatorial ring is redshifted by 10–20 km s^{-1} , as was seen in the higher-resolution echelle spectra of Smith et al. (2007). Also, the entire ring centroid is redshifted by $\sim 20\ \text{km s}^{-1}$ (the dashed line shows $v = 0$ for $H\alpha$), confirming the systemic-velocity measurement by Smith et al. (2007). As noted by those authors, this favours a large Galactic distance on the far side of the Carina spiral arm at 6–7 kpc (similar to well-known supergiants like AG Car and HR Car, as well as the cluster

Westerlund 2, etc.), rather than a closer distance that would put SBW1 inside the Carina Nebula at 2.3 kpc.

Figure 3a reveals no continuum emission in the interior parts of the ring. This means that even though there is dust located there (as indicated by mid-IR thermal emission; see below), the dust does not contribute enough scattered light to affect the $H\alpha$ *HST*/WFC3 image. We can therefore assume that gas in the ring's interior is ionised, and that the corresponding $H\alpha$ emission measure provides information about the electron density in that region (the [S II] lines are detected at too low signal-to-noise ratio in our STIS spectra to use their flux ratio as an electron-density diagnostic).

The continuum-subtracted intensity tracings in Figure 3b reveal no significant difference in the $H\alpha$ /[N II] flux ratio across the ring, consistent with WFC3 imaging as noted above. This suggests that nitrogen abundances and ionisation/excitation conditions are the same in the dense equatorial ring and in the more diffuse gas that fills its interior. It is therefore likely that the roughly solar values for the nebular N abundance derived by Smith et al. (2007) from ground-based spectra with lower spatial resolution apply across the entire nebula.

2.3 Spitzer IRAC and MIPS Images

The position of SBW1 was observed as part of the *Spitzer Space Telescope* (*Spitzer*) survey of star formation in the Carina Nebula (P.I.: Smith; see Smith et al. 2010b) using both the Infrared Array Camera (IRAC; Fazio et al. 2004) and the Mid-Infrared Photometer for *Spitzer* (MIPS; Rieke et al. 2004). Figure 4 shows individual images in the four IRAC bands, the $24\ \mu\text{m}$ MIPS image, and a colour composite of the IRAC images (note that the longer-wavelength 70 and $160\ \mu\text{m}$ MIPS images were saturated). More details about the observations and data reduction are provided by Smith et al. (2010b) and Povich et al. (2011).

SBW1 is clearly detected in all five filters observed by *Spitzer*, and photometry is listed in Table 2. In IRAC bands 1–3, the point-like central star dominated the total flux from SBW1, although low-level extended emission is seen in all three filters consistent with a few percent of the total flux, and the relative contribution of the extended emission increases toward longer wavelengths. The spatial extent of this extended emission in IRAC Bands 1–3 is consistent with emission from the dense equatorial ring seen in *HST* images, and the emission mechanism may be a combination of polycyclic aromatic hydrocarbon (PAH) emission, free-free, and scattered starlight. No spectrum of the 3–6 μm IR emission is available, however.

Extending to longer wavelengths in IRAC Band 4 at $\sim 8\ \mu\text{m}$, the emission is qualitatively different. The emission is no longer dominated by an unresolved point source, but instead appears elongated by a few arcseconds in the SE/NW direction, consistent with the major axis of the nebula. While clearly not a point source, the Band-4 emission is less spatially extended than the ring emission seen in Bands 1–3, although the poorer angular resolution of *Spitzer* at $\sim 8\ \mu\text{m}$ does not clearly resolve the structure of the emitting region. This $\sim 8\ \mu\text{m}$ emission likely arises from thermal emission from hot dust that fills the interior regions of the ring. This emission is seen more clearly in the Gemini/T-

ReCS images presented below. It is also evident from an analysis of the spectral energy distribution (SED) in §2.5 that the $\sim 8\ \mu\text{m}$ flux is dominated by the hot-dust component and not any stellar photospheric emission, consistent with this interpretation.

The MIPS $24\ \mu\text{m}$ image of SBW1 is shown in Figure 4e. Examining the raw image, it is evident that the source is slightly elongated along the major axis of the nebula. We have enhanced the contrast of axisymmetric structure in this image by subtracting a smoothed version of the image from the original, and the elongated nature of the source is clear from the contours drawn in Figure 4e. The asymmetry is present on angular scales larger than the diffraction limit of $\sim 7''$. This suggests that much of the $24\ \mu\text{m}$ flux arises from a source larger than the two peaks of hot-dust emission that dominate the $\sim 8\ \mu\text{m}$ flux (as seen in IRAC Band 4), since those features are separated by only $\sim 4''$. Thus, the $24\ \mu\text{m}$ flux arises largely from cooler dust in the outer equatorial ring, and not from the diffuse emission interior to the ring. This conclusion is supported by our analysis of higher-resolution ground-based mid-IR images in the next section.

2.4 Gemini South/T-ReCS Images

We obtained images of SBW1 at 8.8, 11.7, and $18.0\ \mu\text{m}$ on 2008 March 30, 2009 April 18 and June 9, and 2010 March 29 using T-ReCS mounted on the 8 m Gemini South telescope (see Table 1). T-ReCS was the facility mid-IR imager and spectrograph at Gemini South, with a 320×240 pixel Si:As IBC array, a pixel scale of $0''.089$, and a resulting field of view of $28''.5 \times 21''.4$. The observations were taken with a $15''.0$ east-west chop throw. Individual sky-subtracted frames were then combined to make a coadded image in each filter. Figure 5 shows the resulting coadded T-ReCS images at 8.8, 11.7, and $18.0\ \mu\text{m}$, compared to the *HST*/WFC3 $H\alpha$ image on the same scale (Figure 5a). The left column displays the images in false colour, whereas the right column gives the same images with contours of the $H\alpha$ emission superposed in order to show the relative positions of the ionised equatorial ring and the hot inner dust traced by mid-IR emission.

A point source at the location of the central star is clearly detected at 8.8 and $11.7\ \mu\text{m}$. Both the 8.8 and $11.7\ \mu\text{m}$ images were taken under nonphotometric weather conditions, and the $11.7\ \mu\text{m}$ images were taken over two separate epochs, so we do not use them to derive *absolute* photometry. However, the resulting images can be used to provide a precise measurement of the *relative* contribution of the central point source to the total flux in each filter. We find that the central star contributes $2.5\% \pm 0.2\%$ of the total $8.8\ \mu\text{m}$ flux measured in a $5''$ -radius circular aperture, and similarly, the central star contributes $0.6\% \pm 0.08\%$ of the total $11.7\ \mu\text{m}$ flux measured in a $7''$ -radius circular aperture (a larger aperture was used to measure the $11.7\ \mu\text{m}$ total flux because the $11.7\ \mu\text{m}$ emission is more extended, with some contribution from the main equatorial ring). The central star is not detected in the $18\ \mu\text{m}$ filter. The fractions of the total flux contributed by the central point source are useful for our analysis of the SED discussed below (§2.5).

The T-ReCS images also provide critical information about the spatial distribution of warm dust grains in the SBW1 nebula, which is unclear from the lower-resolution

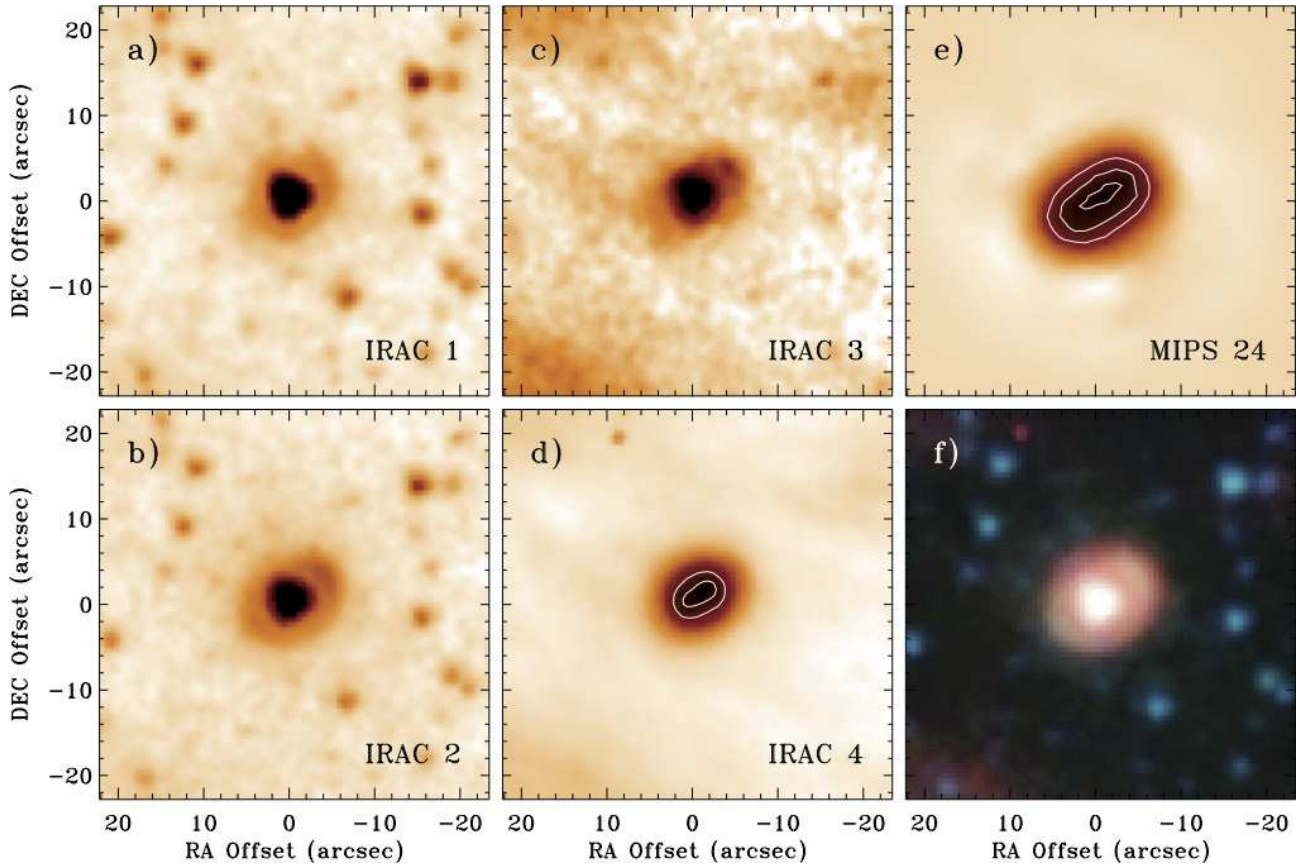


Figure 4. IR images of SBW1 taken with *Spitzer* in (a) IRAC Band 1, (b) IRAC Band 2, (c) IRAC Band 3, (d) IRAC Band 4, and (e) MIPS 24 μm . Panel (f) is a colour composite of IRAC images with Band 1 in blue, Band 2 in green, and Band 4 in red. Contours are drawn to show structure near the emission peak in Panels (d) and (e). The 24 μm image in Panel (e) is displayed to enhance contrast, after having a smoothed version of the image subtracted (a partial unsharp mask). Elongation is apparent in the raw 24 μm image, however.

imaging with *Spitzer*. After separating out the central star, the spatially resolved extended structure seen in the mid-IR can be understood as two spatial components whose relative contribution to the total flux changes with wavelength: (1) emission from the thin equatorial ring with a semimajor axis of $\sim 6''$, whose emission becomes relatively stronger with increasing wavelength, and (2) diffuse emission arising from dust distributed throughout the interior of the ring, but concentrated mainly in two arcs of emission located $2''$ – $3''$ to the SE and to the NW of the central star, whose contribution to the total flux decreases with increasing wavelength. Both the thin equatorial ring and the inner diffuse emission can be seen in the $\text{H}\alpha$ image taken with *HST*. Comparing this $\text{H}\alpha$ emission to the T-ReCS images (right column of Figure 5), it is evident that the equatorial ring contributes no detectable emission to the 8.8 μm image. The outer equatorial ring emission can be seen as a faint halo in the 11.7 μm image, as well as the outer boundary of the (noisy) 18 μm image. This suggests that the equatorial ring contains relatively cool dust. The inner double-peaked structure associated with the more diffuse emission inside the ring dominates the 8.8 and 11.7 μm images, but is less prominent at 18 μm . This suggests that the inner dust is relatively hot.

Tracings of the intensity along the major axis of SBW1 are shown in Figure 6, comparing the *HST* $\text{H}\alpha$ emission to

the mid-IR emission in the three filters observed with T-ReCS at Gemini South (the intensities are scaled arbitrarily for display). These tracings confirm the impression from images that the 8.8 and 11.7 μm flux is dominated by two inner peaks of emission located within $\pm 3''$ from the star. The location of the peak of this emission and the profile shape in tracings at 8.8 and 11.7 μm match, indicating that there is no strong radial temperature gradient in the dust. It is also clear from the tracings in Figure 6 that these two peaks of hot-dust emission coincide with a subtle enhancement of $\text{H}\alpha$ emission. The 18 μm emission has a flatter distribution along the major axis of the nebula, with the flux decreasing only slightly from $2''$ – $6''$ away from the star. Like the equatorial ring seen in $\text{H}\alpha$ by *HST*, the 18 μm emission drops off abruptly at $\sim 6''.5$ from the star (Figure 6), providing strong evidence that cooler dust in the ring emits a considerable fraction of the $\sim 20 \mu\text{m}$ emission. Tracings at all three mid-IR wavelengths show a pronounced deficit of emission within $2''$ of the central star, revealing an inner region devoid of dust grains.

2.5 The SED

Figure 7 shows the SED of SBW1 from optical through IR wavelengths using data from several sources. We ob-

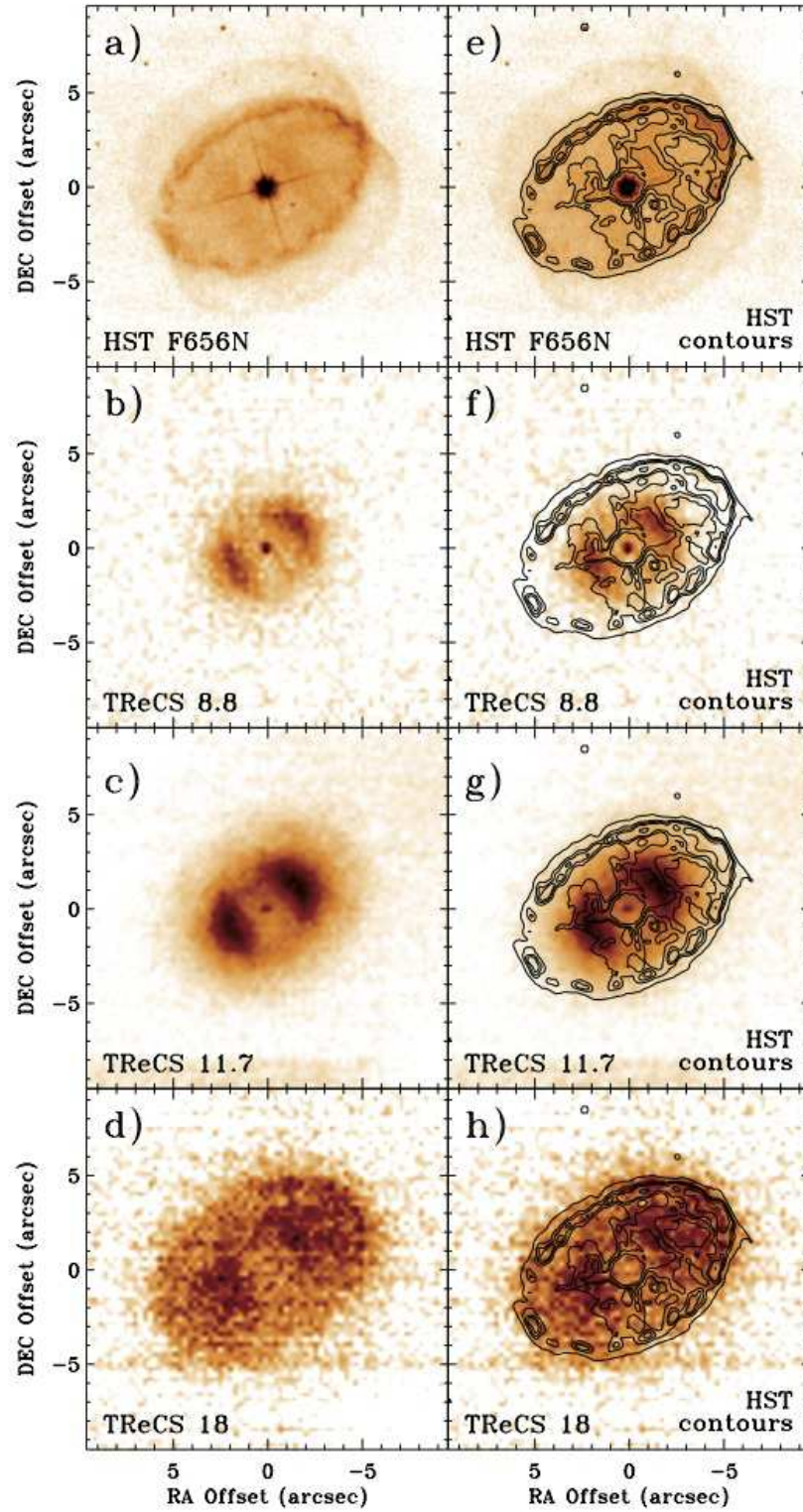


Figure 5. Comparison of thermal-IR images taken with Gemini/T-ReCS and the *HST* image. The left column [panels (a), (b), (c), and (d)] displays the *HST*/WFC3 $H\alpha$ image, and the Gemini/T-ReCS images at 8.8, 11.7, and $18\ \mu\text{m}$, respectively. The right column [panels (e), (f), (g), and (h)] shows the same images with the contours of the *HST* image superposed.

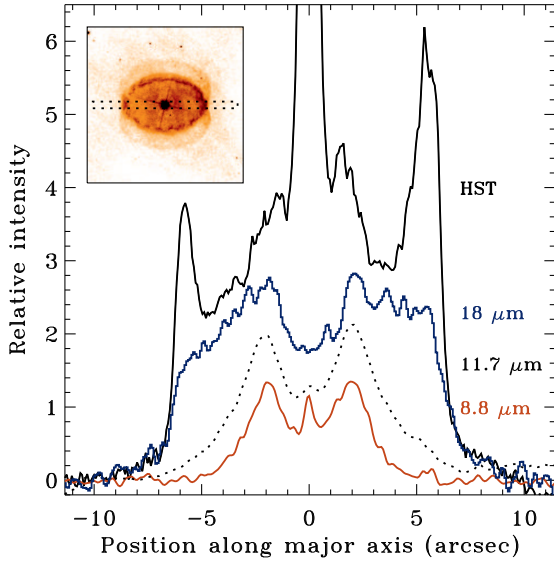


Figure 6. Tracings of the relative intensity across the major axis of the SBW1 ring in the *HST*/WFC3 $H\alpha$ image, and the Gemini/T-ReCS images at 8.8 (red), 11.7 (dotted), and 18 μm (blue). A dashed box in the inset image indicates the location and width of the $1''.5$ -wide scan.

Table 2. Adopted IR flux densities of SBW1

Tel./Instr. ...	Filter/ λ (name or μm)	F_ν (Jy)	\pm (Jy)
2MASS	J / 1.235 μm	0.0959	0.0020
2MASS	H / 1.662 μm	0.0866	0.0019
2MASS	K / 2.159 μm	0.0697	0.0014
WISE	3.4 μm	0.0369	0.0014
WISE	4.6 μm	0.0256	0.0012
WISE	12 μm	0.815	0.038
WISE	22 μm	6.89	0.32
MSX	A / 8.28 μm	0.3034	0.0149
MSX	C / 12.13 μm	1.328	0.0969
MSX	D / 14.65 μm	1.710	0.115
MSX	E / 21.34 μm	6.415	0.398
AKARI	9 μm	0.3102	0.0086
AKARI	18 μm	7.849	0.484
Spitzer/IRAC	3.6 μm	0.039	0.0015
Spitzer/IRAC	4.5 μm	0.032	0.0016
Spitzer/IRAC	5.8 μm	0.027	0.0032
Spitzer/IRAC	8.0 μm	0.209	0.0229
Spitzer/MIPS	24 μm	7.688	1.23

tained publically available IR photometry of SBW1 from the Infrared Science Archive (IRSA¹), including measurements from 2MASS (Skrutskie et al. 2006), and from point-source catalogs of the Midcourse Space Experiment (MSX; Price 1995), Wide-field Infrared Survey Explorer (WISE; Wright et al. 2010), and AKARI satellites. Flux densities (in Jy) from these sources are listed in Table 2, and then converted to νF_ν in Figure 7. We also show V - and R -band photometry from Smith et al. (2007) in Figure 7.

Figure 7 and Table 2 include photometry measured from our *Spitzer* IRAC and MIPS surveys of the Carina Nebula (Smith et al. 2010b). Filled blue circles in Figure 7 correspond to total fluxes of SBW1 measured in a $12''$ -radius

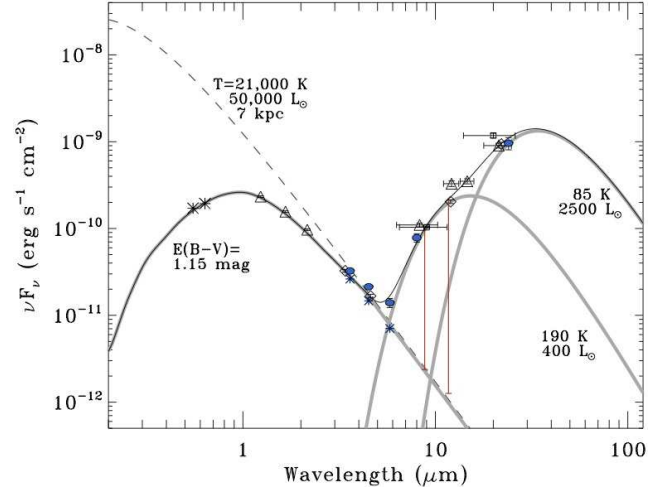


Figure 7. The optical/IR SED of SBW1. The optical V and R magnitudes (asterisks) are from Table 1 of Smith et al. (2007). JHK magnitudes from 2MASS are shown with unfilled triangles. Unfilled diamonds, triangles, and squares show catalog photometry from WISE (3.4, 4.6, 12, and 22 μm), MSX (8.3, 12.1, 14.7, and 21.3 μm), and AKARI (9 and 18 μm), respectively. These all represent the spatially unresolved total flux of the star and nebula. The filled blue dots represent photometry of the entire object from our *Spitzer* IRAC and MIPS data, whereas the blue asterisks represent the measured flux of the central star in the IRAC images in Bands 1–3. Finally, the orange vertical bars represent the flux of the central star in our 8.8 and 11.7 μm T-ReCS images, where we measured the fraction of the total flux contributed by the central point source and then scaled the total flux to match the SED (the images were obtained in some non-photometric conditions). The dashed curve shows a $T = 21,000$ K blackbody, representative of the unreddened B1.5 Iab supergiant. The three thick grey curves are this stellar blackbody reddened by $E(B-V) = 1.15$ mag, plus two grey bodies (emissivity $\propto \lambda^{-1}$) representing thermal emission from dust at approximately 190 K and 85 K. The solid black curve is the total flux contributed by the sum of these three components.

circular aperture in all 5 bands, while blue asterisks are the stellar flux in Bands 1, 2, and 3 measured in a $3''$ -radius aperture with corrections for point-spread function (PSF) flux outside this radius.

Lastly, the long vertical red/orange bars in Figure 7 are derived from the fraction of the total flux contributed by the central star in our 8.8 and 11.7 μm T-ReCS images of SBW1 from Gemini South. The upper end of these bars is tied to the solid-curve fit to the SED (see below), and the bottom of each then represents the expected stellar flux at each wavelength.

As shown in Figure 7, the observed optical and IR photometry of SBW1 can be approximated reasonably well with three simple emission components: (1) a 21,000 K blackbody corresponding to the B1.5 Iab central star (dashed curve), reddened by foreground extinction of $E(B-V) = 1.15$ mag, (2) a greybody (with an emissivity proportional to λ^{-1} at long wavelengths) representing warm dust at 190 K, and (3) another greybody representing cooler dust at 85 K. At a distance of 7 kpc, these stellar-photosphere, hot-dust, and cool-dust components have luminosities of 50,000 L_\odot , 400 L_\odot , and 2500 L_\odot , respectively.

¹ <http://irsa.ipac.caltech.edu/Missions/missions.html>

Photometric information for the unresolved central star is consistent with reddened photospheric emission at all wavelengths up to $\sim 12 \mu\text{m}$. There is no evidence for thermal free-free emission from an extended wind photosphere (e.g., Wright & Barlow 1979) at these wavelengths, implying a rather weak stellar wind from this B 1.5 Iab supergiant. The uncertainty suggests that the free-free stellar wind emission at $\sim 10 \mu\text{m}$ is less than about 10% of the stellar flux, which in turn is 0.5–1% of the total observed flux from SBW1. This would correspond to a flux density of roughly 0.5–1 mJy or less at $10 \mu\text{m}$ for any stellar-wind emission. Using this IR flux and a distance of 7 kpc in Equation (45) of Puls et al. (2008), we find a likely upper limit to the central star’s mass-loss rate of

$$\dot{M} < 4 \times 10^{-7} (v_{300}) (F_{10} D_7)^{3/4} \text{ M}_{\odot} \text{ yr}^{-1}, \quad (1)$$

where v_{300} is the terminal speed of the BSG wind in units of 300 km s^{-1} , F_{10} is the $10 \mu\text{m}$ flux density in mJy (the relevant flux is 0.5–1 mJy), and D_7 is the distance relative to 7 kpc. This upper limit of $\dot{M} < (2\text{--}4) \times 10^{-7} \text{ M}_{\odot} \text{ yr}^{-1}$ for the mass-loss rate of the central blue supergiant star of SBW1 could be a factor of a few lower if the likely effects of clumping are included. In any case, this upper limit is in good agreement with upper limits to the mass-loss rate of SN 1987A’s progenitor of $(1.5\text{--}3) \times 10^{-7} \text{ M}_{\odot} \text{ yr}^{-1}$ inferred from hydrodynamic simulations of the nebula (Blondin & Lundqvist 1993; Martin & Arnett 1995) and an estimated mass-loss rate of $7.5 \times 10^{-8} \text{ M}_{\odot} \text{ yr}^{-1}$ inferred from the observed expansion rate of the radio photosphere (Chevalier & Dwarkadas 1995).

The sharp increase in total flux from 6 to $8 \mu\text{m}$, as the SED transitions from a photosphere to warm-dust emission, is indicative of a cavity with little or no dust close to the star. The 190 K “hot”-dust component dominates the total flux from about 6 to $15 \mu\text{m}$, and arises from the diffuse structures filling the interior of the ring, as seen in the double-peaked feature in the 8.8 and $11.7 \mu\text{m}$ images from Gemini South (Figure 5). The cooler 85 K dust component dominates the total flux longward of about $18 \mu\text{m}$, and this cooler dust appears to reside primarily in the equatorial ring. We cannot rule out the presence of some cooler dust that may produce excess far-IR luminosity (and much higher mass) from presently available data.

One can calculate the approximate mass of dust grains required to emit each of these two components by making some simplifying assumptions about the grain-emissivity properties, and taking the mid-IR emission to be optically thin. Following Smith et al. (2003), the total mass of emitting dust can be expressed as

$$M_d = \frac{4D^2 \rho (\lambda F_{\lambda})}{3 (\lambda Q_e / a) B_{\lambda}(T)}, \quad (2)$$

where $(\lambda Q_e / a)$ is a quantity that describes the grain-emission efficiency Q_e (see Draine & Lee 1984). We assume a distance $D = 7 \text{ kpc}$ for SBW1, and astronomical silicate with a typical grain density $\rho = 3 \text{ g cm}^{-3}$ (at these wavelengths the assumed grain radius is not critical as long as the typical grains are less than $a = 5 \mu\text{m}$). With these parameters we derive dust masses of $M_d(190) = 1.3 \times 10^{-5} \text{ M}_{\odot}$ and $M_d(85) = 4.7 \times 10^{-3} \text{ M}_{\odot}$ for the $T_d = 190 \text{ K}$ and 85 K components of the SED in Figure 7, respectively.

The typical uncertainty for this type of rough estimate

of the dust mass is $\pm 30\%$, dominated by assumptions about grain properties, as well as uncertainties in the ranges of temperatures that can fit the SED. We have assumed astronomical silicate as the nominal dust composition, which seems the most reasonable given that SBW1 is a massive evolved star with normal CNO chemical abundances (Smith et al. 2007). Moreover, IR spectra of SN 1987A obtained with *Spitzer* revealed strong silicate emission features (Bouchet et al. 2006). Unfortunately, we do not have direct observational constraints on the grain composition in SBW1. Had we instead adopted the assumption of small ($a = 0.2 \mu\text{m}$) graphite grains and calculated the dust mass following the method described by Smith & Gehrz (2005), we would have derived dust masses of $M_d(190) = 1.1 \times 10^{-5} \text{ M}_{\odot}$ and $M_d(85) = 8.7 \times 10^{-3} \text{ M}_{\odot}$ for the $T_d = 190 \text{ K}$ and 85 K components, respectively. The mass for the warmer component agrees within the expected uncertainty with that derived above for silicates. The cooler component is a factor of ~ 2 larger for carbon grains, but as noted above, carbon grain composition seems unlikely since SBW1 is not C-enriched. In any case, we regard the value of $M_d(85) = 4.7 \times 10^{-3} \text{ M}_{\odot}$ as a lower limit to the possible dust mass, since our observations do not constrain the SED longward of $24 \mu\text{m}$, making it possible that a larger mass of cooler ($T_d < 85 \text{ K}$) dust might reside in the equatorial ring, or just outside it.

To extend this dust mass to a total nebular mass requires an assumption of the gas-to-dust mass ratio, which is poorly constrained but generally taken to be about 100:1 in massive-star nebulae (see, e.g., Smith et al. 2003, and references therein). We thus infer a total gas mass of order 0.5– 1 M_{\odot} for the ring nebula around SBW1, derived from the mass of the coolest dust we detect. Although the gas:dust ratio could be substantially larger for the hotter 190 K dust component that is mixed with ionised gas in the interior region of the ring, this component makes a negligible contribution to the total nebular mass. Interestingly, a mass of order 0.5– 1 M_{\odot} for the SBW1 ring nebula is about equal to the mass of pre-SN ejecta surrounding SN 1987A. The directly observed mass of ionised gas in the SN 1987A ring is at least 0.04 M_{\odot} , although this is a lower limit to the nebula mass because it is derived from emission lines and corresponds only to a thin skin at the inward-facing edge of the ring that was ionised by the SN; observations of light echoes reveal a much larger mass of material in the ring and outside it of $\sim 1.7 \text{ M}_{\odot}$ (Sugerman et al. 2005).²

The cool-dust component that dominates the $\lambda > 20 \mu\text{m}$ emission has a total luminosity that is $\sim 5\%$ of the original stellar luminosity. The vertical thickness of the dust in the equatorial ring must therefore be $\sim 10\%$ of its radius, or $6 \times 10^{16} \text{ cm}$, based on the fraction of the total luminosity that it intercepts. The much lower luminosity of the hot-dust component, despite its closer separation from the central star, means that it is very optically thin, and so its relative luminosity cannot provide a meaningful constraint on the vertical thickness of this hot-dust component.

² Note that the lower dust mass and higher dust temperature derived from recent observations of the SN 1987A ring by Bouchet et al. (2006) correspond to a very different physical regime of dusty gas that is heated and partly destroyed by the SN shock, so these do not necessarily reflect the properties of dust originally surrounding the progenitor.

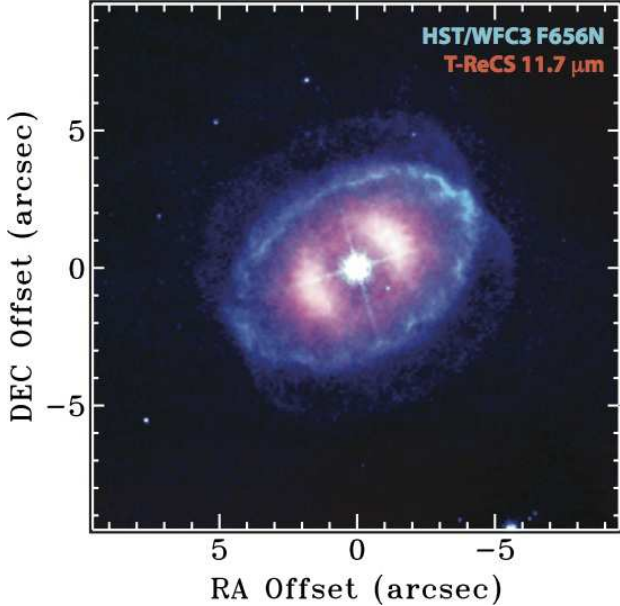


Figure 8. A colour composite of the *HST*/WFC3 F656N image from Figure 5a displayed in blue/green, and the T-ReCS 11.7 μm image from Figure 5c displayed in red/orange.

2.6 X-ray Emission

The Carina Nebula was observed as part of a large program with the *Chandra X-ray Observatory*, called the *Chandra Carina Complex Project* (Townsend et al. 2011). There is no X-ray source listed in the resulting catalog of X-ray sources in this survey (Broos et al. 2011) within a radius of 15'' from SBW1's position. The quoted completeness limit of this survey would suggest an absorption-corrected upper limit to the X-ray luminosity of $10^{30.7} \text{ erg s}^{-2}$ for sources within the Carina nebula region. It is, however, difficult to place a meaningful upper limit on the intrinsic soft X-ray luminosity of SBW1, since it is located at a distance of 7 kpc, far behind the Carina nebula ($D = 2.3 \text{ kpc}$; Smith 2006). Thus, there could be a large absorption column, and its intrinsic soft X-ray luminosity could be substantially higher than this nominal upper limit.

3 OBSERVED MULTI-WAVELENGTH STRUCTURE

Figure 8 shows the relative spatial distribution of ionised gas and warm dust in colour, with the $\text{H}\alpha$ image tinted as blue/green and the mid-IR emission tinted as red/orange. This image encapsulates the basic multiwavelength structure of SBW1, and is useful in the discussion below. One of the curious things about Figure 8 is that it runs counter to normal expectations that dusty regions will be farther from the source of radiation than the ionised gas. This and other issues are clarified below.

3.1 Detailed Structure of the Dense Equatorial Ring

The new *HST*/WFC3 images in $\text{H}\alpha$ and $[\text{N II}]$ provide a detailed view of the morphology in the ring nebula around SBW1. To the extent that SBW1 is a suitable analog, these images also provide our best view of the circumstellar environment around an object like SN 1987A. The most prominent feature in the images is a thin ring of emission, presumably in the equatorial plane. The new *HST* images also provide a better view of the outer rings or hourglass structure in SBW1, and they clarify the nature of the diffuse emission structures in the ring's interior, closer to the central star. Below we examine the structure of the ring in detail, and then conduct a comparison with the equatorial ring of SN 1987A. Structures inside the ring are discussed in the following section.

In general, the equatorial ring around SBW1 appears as a fragmented chain of clumps or filaments with a thin radial extent. Filaments in the ring are marginally resolved with a thickness of $\sim 0''.1$, or 0.0034 pc at a distance of 7 kpc. By assuming this as a typical thickness for the ionised emitting layer, we can provide a rough estimate of the density of ionised gas in the ring from the $\text{H}\alpha$ emission measure, $EM = \int n_e^2 dl$. This can be conveniently expressed (see Smith et al. 2010a) as

$$n_e = 15.0 \sqrt{\frac{I_{\text{H}\alpha}}{L_{\text{pc}} f}} \text{ cm}^{-3}, \quad (3)$$

where $I_{\text{H}\alpha}$ is the $\text{H}\alpha$ line intensity measured in our narrow-band F656N WFC3 image in units of $10^{-15} \text{ erg s}^{-1} \text{ cm}^{-2} \text{ arcsec}^{-2}$, L_{pc} is the emitting path-length through the filament in pc, and f is a geometric filling factor. Based on the clumpy structure in images, we adopt $f = 0.5$. Although this assumption dominates the uncertainty, it is difficult to quantify. We adopt a $\pm 25\%$ uncertainty in the value of f , which translates to a $\pm 11\%$ uncertainty in the resulting value of n_e . In our F656N image (note that the F656N filter on WFC3 includes only $\text{H}\alpha$, and not $[\text{N II}] \lambda 6583$), we measure an intensity of $6.70 \times 10^{-17} \text{ erg s}^{-1} \text{ cm}^{-2} \text{ arcsec}^{-2}$, which translates to $9.7 \times 10^{-16} \text{ erg s}^{-1} \text{ cm}^{-2} \text{ arcsec}^{-2}$ after correcting for $E(B-V) = 1.15 \text{ mag}$ (see Figure 7). With these values, we find $n_e = 370 \pm 40 \text{ cm}^{-3}$. As an independent estimate, from the $[\text{S II}] \lambda \lambda 6717, 6731$ flux ratio measured in ground-based spectra we found $n_e \approx 500 \text{ cm}^{-3}$ (Smith et al. 2007), with a likely uncertainty of $\pm 20\%$. These two estimates are not too discrepant, given the uncertainties. By assuming that the toroidal geometry of the ring is filled with the average of these two density estimates, we would derive a likely mass of emitting ionised gas of $0.012 M_{\odot}$ (see Smith et al. 2007).

This estimate of the mass of ionised gas is much less than the expected total mass of H gas. The ring's dust mass of $5 \times 10^{-3} M_{\odot}$ measured from the luminosity of $\sim 85 \text{ K}$ dust in the SED (see §2.5; Figure 7) would imply a total gas mass of roughly $0.5 M_{\odot}$ if the equatorial ring has a normal gas:dust mass ratio of 100:1. This implies that the ionisation fraction of the ring is only a few per cent. The equatorial ring is therefore ionisation bounded, with the location of the ionisation front determined by the flux of ionising photons from the central star as well as the initial density structure of the ring. The incomplete ionisation of the ring has a strong

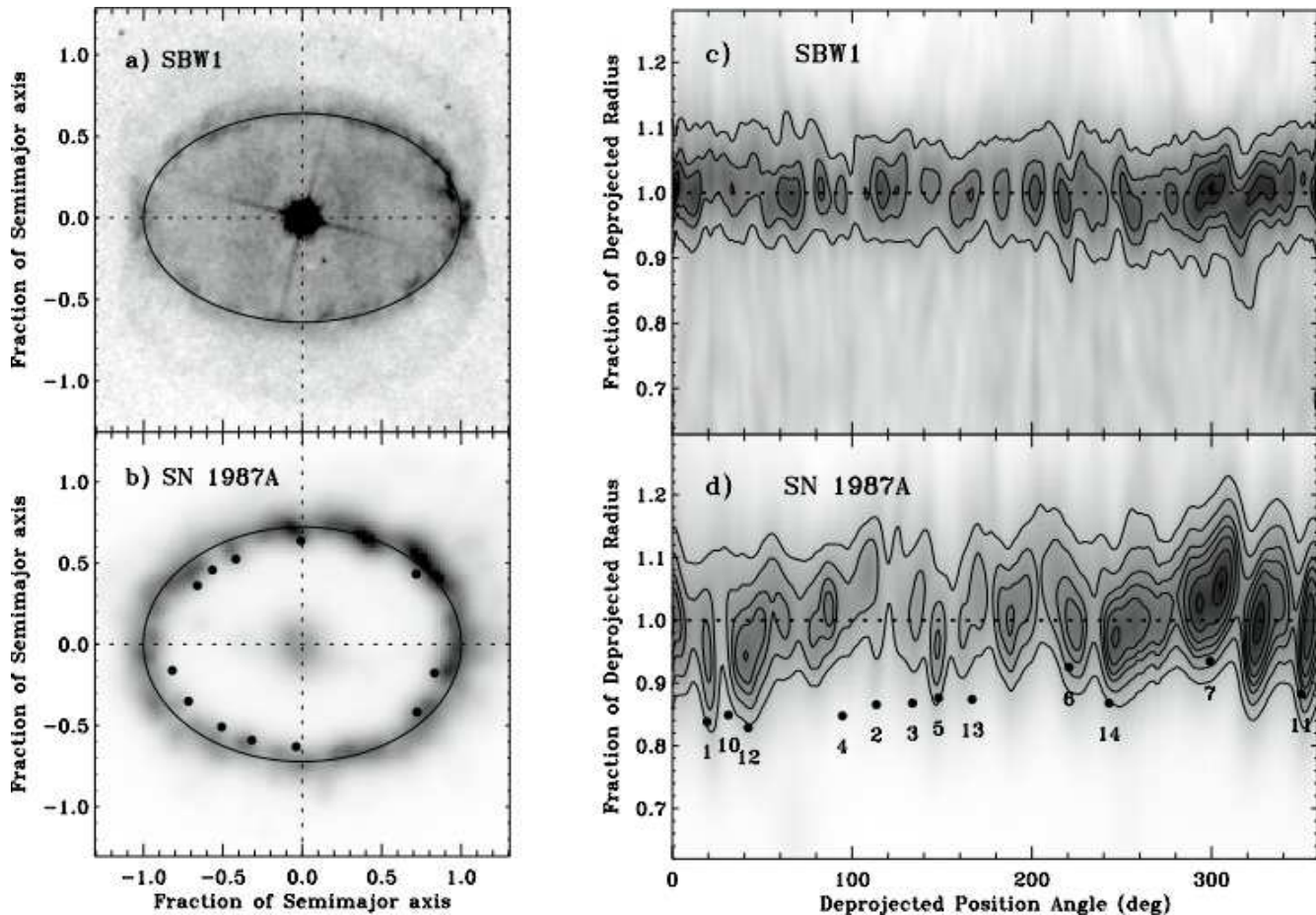


Figure 9. Panels (a) and (b) show $H\alpha$ images of the equatorial rings surrounding SBW1 and SN 1987A, with best-fit ellipses drawn over the images, and rotated so that the major axes are horizontal. The *HST* image of SN 1987A is from Sugerman et al. (2002), and the black dots in panel (b) mark the locations of hotspots from Table 2 of Sugerman et al. (2002). Panels (c) and (d) show the observed $H\alpha$ intensity in terms of deprojected radius from the central object, plotted against the deprojected position angle. Panel (d) is essentially the same as Figure 7c in Sugerman et al. (2002), and panel (c) is plotted the same way for comparison.

impact on the shape of the rest of the nebula around SBW1, and we return to the issue in §4.1 and §4.2.

A strong increase in the ionising flux would be expected to ionise a larger fraction of the total mass in the ring, and would affect the apparent-brightness structure of the ring. This may account for some of the observed morphological differences between SBW1 and the ring of SN 1987A, because the ring around SN 1987A is viewed after a huge burst of ionising radiation from the UV flash of the SN. For example, currently the diffuse gas that fills the interior of the SBW1 ring is bright compared to the thin ring itself, making SBW1 appear more filled-in than SN 1987A (see Figure 9). If the ionising flux of SBW1 were to increase suddenly, we would expect the thin equatorial ring to get much brighter, because more of the high-density neutral gas in the ring would be ionised and the emission measure (proportional to n_e^2) would rise, whereas the interior of the ring would not brighten because it is already fully ionised. Given the difference in ionising flux, however, the morphologies of the two rings are already strikingly similar.

Figure 9 shows $H\alpha$ images of the equatorial rings around both SBW1 and SN 1987A, as well as plots of the depro-

jected intensity around the equatorial ring for each source. These were produced by first fitting an ellipse to the *HST* image of each ring, and then “deprojecting” the appearance of the source by stretching the image by the appropriate factor along the minor axis, in order to make that ellipse into a circle. The deprojected intensity plots in Figure 9 are then a radial tracing of the intensity at all position angles around the ring. For SN 1987A, this is meant to duplicate the analysis by Sugerman et al. (2002), which provides a basis for comparison. We then performed the same analysis for SBW1. For SN 1987A we adopted a ring inclination of $i = 43^{\circ}.8$ (Sugerman et al. 2002), and for SBW1 we measured $i = 50^{\circ}.6 \pm 0^{\circ}.6$, in agreement with an earlier estimate of $i = 50^{\circ}.2 \pm 1^{\circ}$ from a ground-based image (Smith et al. 2007).

Figures 9c and 9d are surprisingly similar. If we characterise the ring structure as dominated by a number of beads along a string, we see that both the wiggles in the string ($\Delta r/R$) and rough angular scale ($\Delta l/R$) of the beads are similar in the two objects, where R is the average ring radius (0.21 pc for SN 1987A and 0.19 pc for SBW1; see Smith et al. 2007). The small variations in Δr are typically about

$\pm 4\%$ of R for SBW1 and $\pm 6\%$ of R for SN 1987A, with a few features reaching inward to 85% of R for both objects. The angular scale of clumps appears somewhat larger for SN 1987A in these figures, but this depends on the effective spatial resolution, which is slightly higher for SBW1 because it is closer (we have smoothed the SBW1 image by about a factor of 3, but it is a factor of 7 closer). A typical separation between major clumps in the ring is 8° to 15° for both, with roughly 22 to 25 major clumps around each ring. Note that these figures are intended to exaggerate the differences in structure between the two rings, with only a portion of R being plotted.

The main interesting result of this analysis is that if we allow for some small differences in spatial resolution and the precise arrangement of blobs, the equatorial ring around SBW1 is for all practical purposes indistinguishable from that around SN 1987A, in terms of its basic physical attributes. Yet, SBW1 is a factor of 7 closer to us, and so in the original *HST* image we have 7 times better effective spatial resolution and can see more details of the structure than for SN 1987A. The chief reason this is interesting is that SBW1 *does not exhibit the long R-T fingers* envisioned for SN 1987A in order to explain the occurrence of hotspots when the tips of the R-T fingers were hit by the blast wave. Instead, SBW1 appears to be a fragmented, clumpy ring with a small radial extent. Since R-T fingers are expected to mark the contact discontinuity between the faster BSG wind and the slower and flattened RSG disk wind, the lack of such features carries implications for the formation mechanism of the ring: the ring is probably not formed by a fast BSG wind sweeping into an extended disk. Indeed, after analysing the structures interior to the ring in the next section, we conclude that the expanding BSG wind is not directly interacting with the dense equatorial ring, due to the increased pressure resulting from photoionisation of the ring. The clumpy dense ring must therefore have had a different origin, as we discuss later.

Lastly, we note a possibly interesting feature of the ring morphology. The brightest part of the ring on the north-west edge, at position angle P.A. $\approx 310^\circ$, coincides with a pronounced kink in the ring, exhibiting the largest jump in deviations from the average ring radius (see Figure 9c). The significance or cause of this structure is not obvious. However, a similar kink is seen to be associated with the brightest portions of the ring around SN 1987A as well, coincidentally also located at P.A. $\approx 310^\circ$. One can readily imagine how a single large departure from azimuthal symmetry could arise in a sudden ejection in a binary system, but this is harder to explain when the structure of the ring arises from colliding winds alone (this is discussed in more detail below).

3.2 Structures Inside the Ring

The most unexpected result of this study of SBW1 concerns the diffuse emission from structures in the interior of the equatorial ring. While ground-based $H\alpha$ images revealed some diffuse emission apparently filling the ring interior (Smith et al. 2007), it was difficult to reliably separate contributions from the ring and the stellar PSF. The new *HST*/WFC3 F656N image shows that the distribution is not uniform across the ring; there are two regions of enhanced $H\alpha$ emission located about $1''$ to $3''$ on either side of the

central star, and there is a marked deficit of $H\alpha$ emission within $1''$ to $2''$ of the star (see Figures 1 and 5).

More striking, however, are the high-resolution mid-IR images obtained with T-ReCS on Gemini South. In the mid-IR, we see two distinct peaks of warm-dust emission located $1''$ to $3''$ on either side of the central star, oriented along the minor axis of the ring (see Figures 5 and 8). These dust-emission peaks appear to be spatially coincident with the enhancements of $H\alpha$ mentioned above, but have a much stronger contrast in the mid-IR. The two peaks are probably caused by limb brightening of a toroidal structure with a projected radius of $\sim 2''$, and if they are located in the equatorial plane, these inner dust peaks occur at about $1/3$ of the radius of the dense equatorial ring (which is ~ 0.2 pc; Smith et al. 2007). The IR emission also shows a clear deficit within a few arcseconds of the star, indicating an inner region that is relatively devoid of hot dust.

The double-peaked mid-IR emission has the strongest contrast at the shorter mid-IR wavelengths (8.8 and $11.3 \mu\text{m}$), whereas the emission structure appears more uniform at the longest thermal-IR wavelength ($18 \mu\text{m}$) due to a rising contribution from the outer equatorial ring. This suggests that the double-peaked features have the hottest dust, consistent with their location closer to the star than the other structures. Analysis of the optical/IR SED of SBW1 (Figure 7; §2.5) suggests the presence of two dust components emitting at ~ 190 K and 85 K. The mid-IR images therefore indicate that the warmer 190 K component must be associated with the inner double-peaked emission, and that the cooler 85 K component is associated with cooler dust located in the dense equatorial ring.

That the double-peaked emission inside the ring is seen in both $H\alpha$ and in mid-IR continuum emission suggests that the hot dust is intermixed with ionised gas. In that case, the heating of the dust could be collisions with dust, trapped $\text{Ly}\alpha$ radiation, or direct heating by stellar radiation. The equilibrium grain temperature due only to stellar radiation is given by

$$T_g = 28 \left[\frac{Q_{\text{abs}}}{Q_e} \frac{L}{10^4 L_\odot} \left(\frac{R}{10^4 \text{ AU}} \right)^{-2} \right]^{1/4} \text{ K}, \quad (4)$$

where Q_{abs}/Q_e is the ratio of absorption to emission efficiency for the grains. For blackbodies (i.e., $Q_{\text{abs}}/Q_e = 1$) we would expect a dust temperature around 40 K, adopting a stellar luminosity of $5 \times 10^4 L_\odot$ and separation from the star of 1.5 or $10,500$ AU (assuming a distance of 7 kpc). Instead, the SED indicates relatively hot dust at a temperature of ~ 190 K (Figure 7), which would require Q_{abs}/Q_e to be very large, around 500 . This efficiency could indicate very small grains with radii $< 0.1 \mu\text{m}$, which have very low heat capacity and can be superheated by UV radiation or trapped $\text{Ly}\alpha$. Significant additional heating might also occur from collisions with the ionised gas, because grains that are charged due to the photoelectric effect can have a much larger cross section for collisions with charged particles in ionized gas. A similar temperature difference occurs in the main equatorial ring, where the observed dust temperature of 85 K is much larger than the expected equilibrium blackbody temperature of ~ 20 K. If additional heating from trapped $\text{Ly}\alpha$ or collisions with ionised gas are present, this is important to consider when conducting simple radiative-transfer models of the circumstellar dust emission around luminous stars,

and adds a note of caution for dust properties inferred from those models.

In any case, the exact heating mechanism of the dust interior to the ring is less critical than the fact that it resides there. The existence of dust at this location is problematic for conventional interacting-wind models for the formation of a ring nebula like the one around SN 1987A (Blondin & Lundqvist 1993; Martin & Arnett 1995; Collins et al. 1999; Morris & Podsiadlowski 2009). These models predict that the R-T instabilities in the ring itself mark the contact discontinuity between the BSG wind and a pre-existing disk wind. If so, then the volume interior to the ring should be filled with mass from the BSG wind. There will be a reverse shock somewhere between the star and the ring, but this is not expected to form dust. Steady BSG winds do not form dust on their own, and the SED and spectrum of the central source in SBW1 reveal no evidence for a dusty red giant star in a binary system. Thus, the dust in the interior of the ring around SBW1 must have some other origin, and suggests that a simple interacting-winds model incorporating only hydrodynamic effects must be rejected.

Implications for a possible origin of this structure are discussed in the next section, related to the proposed existence of an ionised portion of a progenitor RSG wind around SN 1987A (Chevalier & Dwarkadas 1995). In short, we propose that the dusty region interior to the SBW1 ring originates from photoionisation and photoevaporation of neutral dusty gas in the dense equatorial ring, which then expands to partially fill the interior region of the ring. This dusty photoevaporative flow meets the expanding BSG wind at a shock interface with a toroidal geometry inside the ring. A sketch of the proposed geometry for SBW1 is given in Figure 10, and is discussed in more detail below.

4 DISCUSSION

4.1 Origin of the Dusty H II Region Inside the Ring: The Role of Ionisation and Photoevaporation

In the previous sections, we have described how observed structural properties of the SBW1 ring seem to be in conflict with some aspects of hydrodynamical models for the formation of SN 1987A’s nebula. Specifically, we highlighted the lack of long R-T fingers and the existence of dust interior to the ring. Both challenge the standard interacting-winds picture where R-T fingers form as a result of instabilities in the contact discontinuity between a fast BSG wind and a flattened disk-like RSG wind. The presence of dust far interior to the ring is extremely important, because it means that the BSG wind (presumably devoid of dust) has not yet reached the ring, and in fact has not even penetrated past about 1/3 the radius of the ring in the equatorial plane.

In this section we suggest a modification to this scenario, wherein ionisation and evaporation of a dense neutral ring produces a photoevaporative flow which, in turn, profoundly influences the overall hydrodynamics and shaping of the nebula. These ionisation effects have so far been neglected in numerical simulations, but we argue that they are essential, and our intention is that our discussion of the observations will inspire such a numerical study. Our

proposed scenario follows the suggestion by Chevalier & Dwarkadas (1995), who invoked a dense H II region arising from photoionised portions of a previous RSG wind in order to account for some aspects of the advancing blast wave of SN 1987A. The additions and modifications that we make to this scenario concern the dynamical influence of the ionised photoevaporative flow off the ring, the nature of the interaction between this flow and the BSG wind, and the origin of dust in the system (not necessarily from a RSG wind).

In Figure 10 we show a sketch of the proposed geometry for the SBW1 ring and material inside it (this is a side view in the equatorial plane). In brief, the picture we propose is that the warm dust seen in Gemini South/T-ReCS images resides at or near the location of a shock front at the interface where the outflowing BSG wind meets the inward flow of dusty ionised gas that has been photoevaporated from the dense equatorial ring/torus. In a two-dimensional cross section, this structure has a parabolic shape due to the divergent flow from the ring. This is analogous to the opening angle of two colliding winds in a binary system, except here the structure is toroidal rather than a cone, because the source of the flow is a dense ring rather than a companion star. In effect, this ionised photoevaporative flow off the dense equatorial ring is able to keep the BSG wind at bay in the equatorial plane, preventing it from reaching the equatorial ring so that no direct hydrodynamical interaction between the ring and the BSG wind is able to occur. Instead, ionising photons that travel ahead of the shock have the most important dynamical effect because of the increase in pressure when the gas is ionised. The geometry sketched in Figure 10 could arise from a sequence of events such as that described in the following section.

4.2 Formation of the Observed Structure in SBW1

In this section, we outline a possible sequence of events that may have led to the formation of the ring nebula around SBW1. We also discuss the most relevant physical mechanisms for each component of the nebula. The key difference between this and previously suggested scenarios is the hydrodynamic role of an ionised photoevaporative flow off the ring. A key point is that the ionised gas pressure is allowed to have a major impact on the hydrodynamics because of the slow ($10\text{--}20\text{ km s}^{-1}$) initial expansion speed of the dense ring.

4.2.1 Episodic Ring Ejection as a BSG, Not a RSG Disk-Wind

Several previous studies that sought to explain the unusual structure of the nebula around SN 1987A assumed some form of a fast BSG wind ($300\text{--}400\text{ km s}^{-1}$) blowing into a slower RSG wind ($5\text{--}10\text{ km s}^{-1}$). Different versions of this are seen in the more standard “hydrodynamics-only” interacting-winds model (Luo & McCray 1991; Blondin & Lundqvist 1993; Martin & Arnett 1995), as well as in the H II region model of Chevalier & Dwarkadas (1995). In the sections to follow, we argue that the structures observed around SBW1 seem to clearly support the model of Cheva-

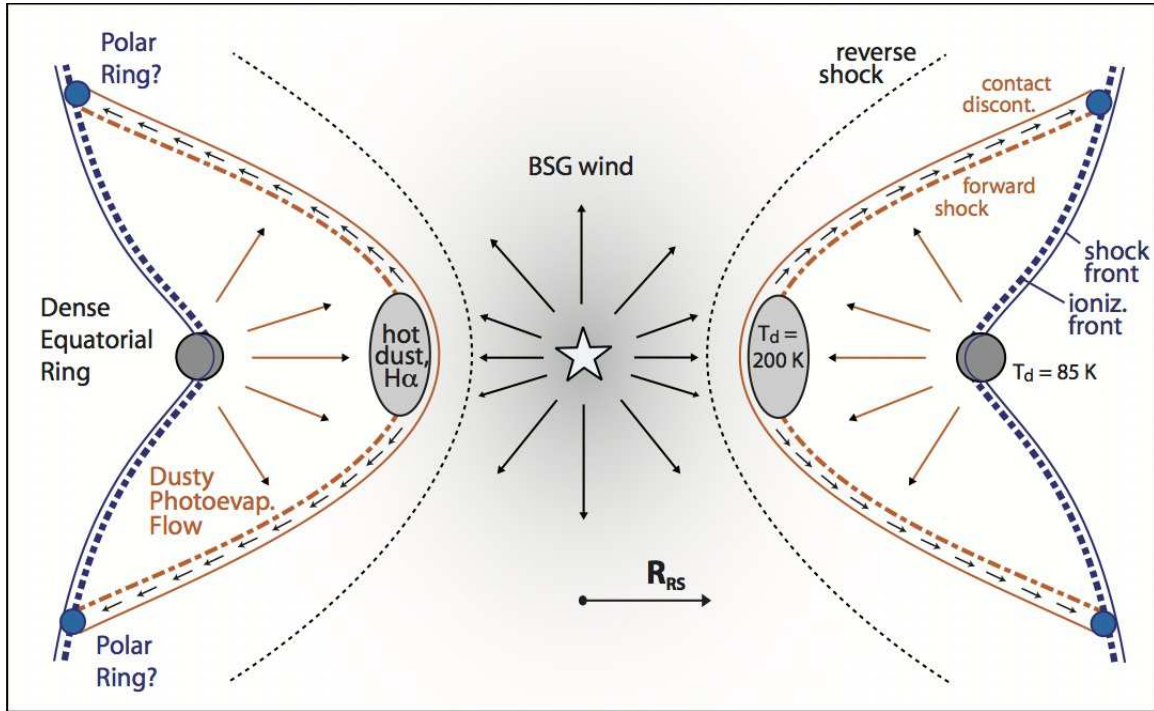


Figure 10. A sketch of the proposed emitting geometry of SBW1. The observed features are the dense equatorial ring, the polar rings, the outer hourglass-shaped shell (dashed and thin solid blue curves), the hot dust and H α that piles up near the contact discontinuity in the equatorial plane, and the central star. Other structures are proposed to explain these observed features as discussed in the text: the BSG stellar wind, the reverse shock in the BSG wind (black dashed), the dusty photoevaporative flow (DPF) off the ring (orange arrows), the forward shock driven into the DPF (dashed orange), and the contact discontinuity between the shocked DPF and the shocked BSG wind (solid orange). The thin solid blue curves represent a weak D-type shock front driven into the neutral ring and outer nebula by the pressure of the ionization front, and the small black arrows represent the accelerated shear flow of the shocked DPF. Relative sizes of various features are meant to demonstrate the general structure, and are not exactly to scale. Whether the polar rings actually arise at the intersection of the outer hourglass-shaped shell and the shocked DPF is unclear from observations; this is a conjecture. With some adaptation in scaling (i.e., opening angle of the reverse shock, latitude of the polar rings, etc.), this same geometry might apply to the nebula around the progenitor of SN 1987A.

lier & Dwarkadas (1995), wherein the effects of photoionization are critical in producing a dense H II region at low latitudes, but allowing the BSG wind to expand freely out the poles. However, one aspect in which our suggested scenario differs from that of Chevalier & Dwarkadas (1995) is in the assumption of a previous RSG wind, as discussed in this section.

The assumption of a previous RSG wind is motivated by the slow ($\sim 10 \text{ km s}^{-1}$) expansion speed in the equatorial ring of SN 1987A. However, this assumption also introduces significant difficulties, as the RSG wind must be concentrated in a thin disk with a very high equator-to-pole density contrast (Luo & McCray 1991; Blondin & Lundqvist 1993; Martin & Arnett 1995). Moreover, these hydrodynamic simulations predict an hourglass structure with complete polar caps, rather than empty polar rings. Since the extended envelope of any single RSG star will have a very low angular velocity, one must invoke some interaction with a companion star in a binary system (possibly even a merger) in any scenario involving a RSG (Collins et al. 1999; Morris & Podsiadlowski et al. 2009).

Yet, if one must invoke a binary system, then a previous RSG phase is not really needed, because a RSG wind is not the only way to form a slowly expanding dusty equato-

rial ring, and moreover, such a flattened disk-like outflow has never been observed around a RSG (binary or single). A different case that has well-established observational and theoretical precedent is the episodic ejection of a ring by a BSG. This could have been the result of a binary merger event (Morris & Podsiadlowski 2009), an episodic ejection event occurring during Roche-lobe overflow (RLOF) as seen in the eclipsing binary RY Scuti (Smith et al. 2011), or an eruptive ejection from a rotating star (Smith & Townsend 2007; Shacham & Shaviv 2012). In either a binary merger event or accretion from a companion in RLOF, a large amount of angular momentum must be shed in order for material to be accreted onto the merger product or the mass-gaining star, respectively, and one thus expects the mechanical mass shedding to occur in the equator. If the mass loss is episodic, this brief equatorial ejection will form a ring rather than an extended disk because of the brief nature of the mass ejection. Shedding of mass at the equator in this way forms a nearly Keplerian ring with a relatively slow radial expansion speed, which can be much less than the escape speed from the surface of a BSG star.

A prime example of the scenario we suggest is seen in the Galactic eclipsing binary system RY Scuti, in which an OB supergiant binary system undergoing RLOF has re-

cently ejected a ring/torus that is spatially resolved in *HST* images (Smith et al. 1999, 2002, 2011). The radial expansion speed of the equatorial ring/torus in RY Scuti is only 30–40 km s⁻¹ (Smith et al. 2002), much less than the several hundred km s⁻¹ escape velocity or wind speed from the O9/B0 supergiant stars. Moreover, this has occurred without a RSG phase, because the stars are too close together with an orbital period of only ~ 11 days (Grundstrom et al. 2007; Smith et al. 2002, and references therein). RY Scuti is an important example, because measured proper motions of the very young (120 yr old) nebula show that the equatorial mass loss was the result of a pair of *brief episodic ejections* rather than a steady flow of mass from the equator (Smith et al. 2011).

Moreover, the nebula around RY Scuti reveals that the slow equatorial outflow led to the formation of significant amounts of dust (Gehrz et al. 2001), even though it is a binary composed of two hot OB supergiants. In fact, episodic or eruptive mass loss like that seen in luminous blue variables (LBVs) may be an essential ingredient for the formation of dust around BSG stars, as discussed in detail recently by Kochanek (2011). The class of B[e] supergiant stars provides many additional examples of BSG stars that have formed significant quantities of dust in a slowly expanding equatorial ring or torus (e.g., Zickgraf et al. 1996). *Thus, the formation of a slow and dusty equatorial ring does not require a previous RSG phase.* In fact, of the three known Galactic analogues of the nebula around SN 1987A (these are HD 168625, Sher 25, and SBW1), two (Sher 25 and SBW1) have chemical abundances that are inconsistent with a previous RSG phase (Smartt et al. 2002; Smith et al. 2007). The third analog, HD 168526, is an LBV that has quite likely suffered previous eruptive mass loss (Smith 2007).

What about the observed clumpy structure of the SBW1 ring? As noted above, the dust residing far interior to the ring suggests that the BSG wind has not yet reached the radius of the dense equatorial ring, and as such, the clumps observed in the equatorial ring cannot be the result of R-T instabilities at the contact discontinuity as required in interacting-winds models. We suggest instead that this regular clumpy structure may occur naturally due to thermal instability and fragmentation of an ejected ring, rather than from R-T instabilities. In both SBW1 and SN 1987A, the measured ring expansion speed is 10–20 km s⁻¹, so the initially ionised ring would be expected to fragment as it cools and recombines (and its sound speed drops well below 10 km s⁻¹). Perhaps this fragmentation could lead to the fairly regular series of clumps around the ring in both objects (Figure 9). This is, however, a minor point.

Subsequently, as the BSG star now seen at the centre of SBW1 recovers from the mass-loss event and presumably contracts to become a hotter BSG, its wind speed (escape speed) and its ionising flux could both increase, and their ratio has an important influence on the resulting structure. The influence of photoionisation of the ring ejecta is discussed next.

4.2.2 Photoionisation of the Ring, and a Dusty Photoevaporative Flow

After ejecting a thin equatorial ring, the inner edge of the ring will be exposed to ionising photons from the central

BSG star. Chevalier & Dwarkadas (1995) predicted that photoionisation had a strong impact on the structure interior to the SN 1987A ring, and we suggest a similar process in the case of the observed structure around SBW1.

The central star of SBW1 is a B1.5 Iab supergiant, which should produce an ionising photon flux of roughly $Q_H \approx 10^{48} \text{ s}^{-1}$ (see Martins et al. 2005). This radiation flux ionises the inward-facing surface of the ring at a radius $R \approx 0.2 \text{ pc}$ from the star. In §3.1, we found that the total mass of ionised gas emitting H α was too low, inconsistent with the larger mass we would expect to be associated with the cool 85 K dust in the ring. We therefore conclude that most of the mass in the ring is neutral H residing in high-density clumps in the ring, which must be self-shielded from the BSG star’s ionising radiation. The minimum density n_H required to keep the clumps neutral can be estimated from simple ionisation balance:

$$n_H = \left(\frac{Q_H}{4\pi R^2 \alpha_B L} \right)^{1/2}, \quad (5)$$

where $\alpha_B \approx 3 \times 10^{-13} \text{ cm}^3 \text{ s}^{-1}$ is the Case B hydrogen recombination coefficient and $L = 0.0034 \text{ pc}$ is the same observed depth of the emitting layer of the ring as before. We find an expected density in the ring of $n_e \approx 8500 \text{ cm}^{-3}$. This is more than an order of magnitude higher than the electron densities derived from the [S II] line-intensity ratio and from the observed emission measure of H α (both are discussed above in §3.1), thus confirming that H α and [S II] emission trace only a fraction of the total mass, associated with a thin ionised skin and ionised photoevaporative flow coming off the ring (the rest of the mass remains neutral).

When the neutral gas in the clumps gets ionised, its temperature increases to $\sim 10^4 \text{ K}$ and the overpressure causes the gas to expand away from the dense clump (e.g., Oort & Spitzer 1955). The expansion speed should be of the same order as the sound speed in ionised gas, $c_s \simeq 10 \text{ km s}^{-1}$. This is also comparable to the expansion speed of the ring itself. The photoablation mass-loss rate is roughly

$$\dot{M} = 2\pi R L \mu m_H n_e c_s \quad (6)$$

which is roughly equal to $8 \times 10^{-6} M_\odot \text{ yr}^{-1}$ for the parameters given above. This, in turn, suggests a lifetime for the neutral ring of $6 \times 10^4 \text{ yr}$, longer than the $\sim 10^4 \text{ yr}$ dynamical age of the ring (Smith et al. 2007). The resulting ionised photoevaporative flow is closely analogous to the ionised photoevaporative flows from neutral clouds at the edges of H II regions, as discussed in detail by Bertoldi (1989) and Bertoldi & McKee (1990). A similar role of photoevaporation is at work in the proplyds in the Orion Nebula, as discussed more below.

The originally neutral gas in the dense equatorial ring is mixed with dust. This cool dust resides outside the ionisation front in the ring, and is observed as the $\sim 85 \text{ K}$ component in the IR SED of SBW1 (Figure 7), which is spatially resolved to be coincident with the thin ring in our 18 μm Gemini/T-ReCS image (Figure 5). After being struck by ionising photons, the ionised photoevaporated material from the ring will likely entrain the dust with it as it expands into the interior of the ring. Thus, we refer to the resulting expansion as a dusty photoevaporative flow (DPF) in Figure 10. This dust in the DPF moves inward and eventually piles up at the shock front (discussed in the following section), giving

rise to hot (~ 190 K) dust emission peaks inside the ring that are spatially resolved in Gemini images (Figures 5 and 8). This hypothesis seems far more likely than any alternative explanation for the origin of dust seen interior to the ring in mid-IR images. Such alternatives would require that dust forms quickly in the fast BSG wind and survives passage through the strong (several 10^2 km s $^{-1}$) reverse shock.

This physical situation we propose for SBW1 has an interesting analog in the evaporating protoplanetary disks (the so-called ‘‘proplyds’’) seen in *HST* images of the Orion Nebula (see Bally et al. 1998; Johnstone et al. 1998). In these objects, UV radiation from the nearby O6 V star θ^1 C Ori causes a photoevaporative flow off the dense and dusty protoplanetary disk envelopes that are seen in silhouette. After passing through an ionisation front, the ionised photoevaporative flow continues to expand in a divergent flow until it collides directly with the fast stellar wind of θ^1 C Ori. The proplyds located in the Trapezium very close to θ^1 C Ori show bright arcs of H α emission marking the shock between the ionised photoevaporative flow and the stellar wind (Bally et al. 1998). Interestingly, these same H α arcs are also very bright in the thermal-IR continuum in high-resolution 11.7 μ m images (Smith et al. 2005), indicating the presence of hot dust. Since the wind of θ^1 C Ori is too fast, rarefied, and hot to form dust on its own, the dust in these shocks must have been entrained in the ionised photoevaporative flow from the proplyds. This is akin to the situation we propose for SBW1, except that instead of an externally ionised disk envelope in the Orion proplyds, we have a thin ring illuminated from the inside.

Because of the thin-ring geometry of the neutral gas reservoir, the DPF will expand into the interior of the ring toward the star, but the pressure of the ionised gas will also cause it to expand over a range of latitudes above and below the equator. This will form a thicker torus-like geometry stretching from the equatorial plane to mid latitudes, as depicted by the DPF in Figure 10.

4.2.3 Collision of the DPF and the BSG Wind

The DPF will expand away from the dense equatorial ring, primarily into its interior, until it collides with the outflow from the stellar wind of the central BSG. This collision between the BSG wind and the DPF will have three boundaries: the reverse shock that decelerates the BSG wind, the forward shock driven into the DPF, and the contact discontinuity between them. These are labeled in Figure 10. The zone between the forward shock and contact discontinuity is drawn as a thin region, due to the high-density gas and slow velocity of the forward shock. The region between the contact discontinuity and reverse shock is thicker, due to the higher speed and lower density of the BSG wind.

Consider the balance between the gas pressure of the ionised photoevaporative flow (H II region) and the ram pressure of the BSG wind in the equatorial plane:

$$n_e kT = \frac{\dot{M} V_{\text{BSG}}}{4\pi R^2}, \quad (7)$$

where n_e and T are the ionised gas density and temperature in the H II region, and \dot{M} and V_{BSG} are the mass-loss rate and wind speed of the BSG wind, respectively. While the pressure in the H II region is roughly constant with radius,

the ram pressure of the wind drops with radius from the star if we assume a steady BSG wind (R^{-2} density profile). Then R is the radius where the two balance, given by

$$R = 0.05 \left(\dot{M}_{-7} V_{300} \right)^{1/2} \left(\frac{n_e}{500 \text{ cm}^{-3}} \right)^{-1/2} \text{ pc}, \quad (8)$$

where we have assumed $T = 10^4$ K in the H II region, \dot{M}_{-7} is the BSG wind mass-loss rate in units of $10^{-7} M_{\odot} \text{ yr}^{-1}$, and V_{300} is the wind speed in units of 300 km s $^{-1}$. We derived a density of about 500 cm $^{-3}$ for the ionised gas in the interior of the ring (§3.1), so this is used as a reference value. We derived an *upper limit* to the BSG mass-loss rate of $3 \times 10^{-7} M_{\odot} \text{ yr}^{-1}$ from the IR flux of the central star (§2.5), so $10^{-7} M_{\odot} \text{ yr}^{-1}$ is used as a fiducial value. We assumed a value for V_{BSG} of 300 km s $^{-1}$, as above. These are similar to the values adopted for the progenitor of SN 1987A by Chevalier & Dwarkadas (1995) as well. With these values, the stand-off shock will be at $R \approx 0.05$ pc from the BSG. This is about 25% of the radius of the ring, which roughly matches the location of the hot dust and enhanced H α emission in images, and which we associate with the shock front. The agreement indicates that this interpretation is plausible. An approved program in *HST* Cycle 20 will use the Cosmic Origins Spectrograph (COS) to obtain a UV spectrum of the central star in SBW1, allowing direct estimates of \dot{M} and V_{BSG} .

Since the H II region is toroidal and caused by evaporation of a thin equatorial ring, we expect the density to drop at latitudes above and below the equator because the ionised photoevaporative flow diverges. If so, this would cause the location of the shock front to curve outward to larger radii, as depicted in Figure 10. The variation with latitude is discussed further below.

In the sketch of the geometry shown in Figure 10, mass in the outflowing BSG wind and gas from the ionised photoevaporative flow will both pile up at the shock front. After colliding, the post-shock gas should then flow away from the star, in a nonradial trajectory that follows the geometry of the shock interface (small black arrows in Figure 10). This is analogous to flow down the shock cone in a colliding-wind binary, but here the geometry is toroidal rather than a cone. The material in this post-shock flow is denser than gas in the H II region or the BSG wind. It is this higher-density zone of ionised gas that probably dominates H α emission because of the n_e^2 dependence of recombination emission.

In fact, it seems likely that the dense gas in this post-shock flow has already been observed directly. There is evidence for the resulting nonradial flow in high-resolution, long-slit echelle spectra of H α and [N II] emission in SBW1 that we presented in a previous study (Smith et al. 2007), obtained with the EMMI spectrograph on the NTT. In that paper, we were perplexed by the unusual position/velocity structures, but it now makes sense in the context of the geometry proposed above. In Figure 11 we show the position-velocity diagram of the earlier EMMI echelle spectra of [N II] $\lambda 6583$, presented originally by Smith et al. (2007), as well as a sketch for how these velocity structures may arise from the nonradial flow at the shock interface. While a quantitative test of this idea will require numerical simulations of the hydrodynamics, the cartoon of the nonradial flow trajectories in Figure 11c provides a reasonable explanation for the observed position-velocity structure in Figure 11b.

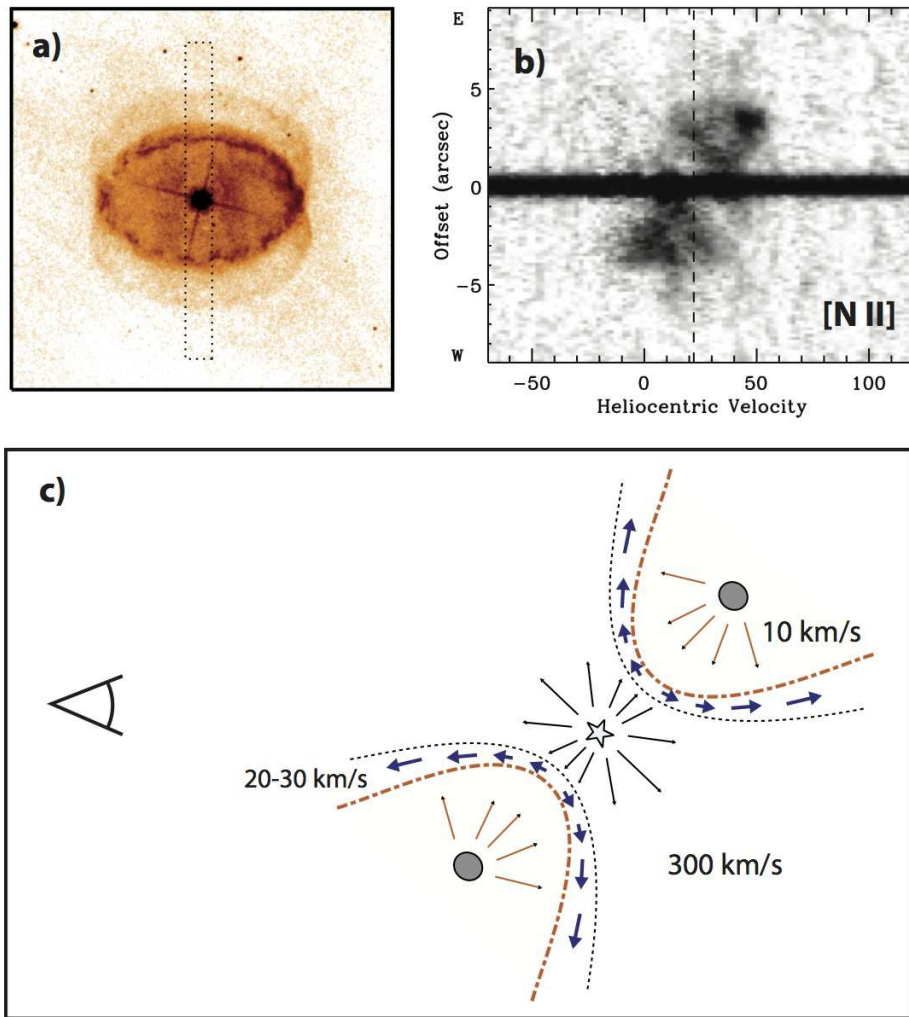


Figure 11. A possible kinematic signature of the latitudinal outflow structure resulting from the collision between the DPF and the BSG wind. Panel (a) shows the approximate slit position for the long-slit echelle spectrum in (b). Panel (b) is the position-velocity diagram for [N II] $\lambda 6583$ from the long-slit echelle spectrum of SBW1, as presented by Smith et al. (2007). (The kinematic emission structure of [N II] is essentially the same as that of H α .) The cartoon in Panel (c) is a simplified version of the sketch in Figure 10, concentrating on the shock interface. Arrows denote the nonradial flow of plasma down the shock, in the dense region between the forward and reverse shocks.

4.2.4 Latitudinal Structure

In both SBW1 and around SN 1987A, *HST* images do not reveal dense nebular material in the polar directions. Rather, the polar rings of SN 1987A are true hollow rings residing at mid latitudes (Burrows et al. 1995; Plait et al. 1995). The same appears to be true based on our *HST* images of SBW1. The lack of any dense polar structures in SBW1 or in SN 1987A argues against a shaping mechanism like the one discussed by Morris & Podsiadlowski (2009), because that formation model predicts dense polar caps in the nebula. The same is true for most of the colliding-wind models that predict complete hourglass shapes (see above), not empty rings at mid latitudes. If such polar caps existed, they would be impacted by the fast polar wind of the BSG, and would likely be swept into a thin dense shell, and this interface would therefore be easy to detect in deep images.

Instead, the empty polar regions favour a different sce-

nario like that suggested by Chevalier & Dwarkadas (1995), which is similar to the picture we advocate here. Rather than a pre-existing disk wind, we have proposed that the central BSG star episodically ejects a dense ring, which is then photoionised as it expands. The ionised gas expands to form a thick torus around the ring, which provides a barrier for the BSG wind. The collision between the wind and the ionised torus (H II region) creates a curved shock front. In this picture, all of the slow and dense material is confined to low latitudes, so that the BSG wind is able to expand with no obstruction out the poles.

Is the BSG wind spherical? Ejection of an equatorial ring requires a system with excess angular momentum, suggesting either a rapidly rotating star or a close binary system. Even in a binary system with RLOF, the mass-gainer star accretes both mass and angular momentum, and would be expected to be in very rapid rotation. The geometry of

the stellar wind from a rapidly rotating hot star is complicated, because hot stars have line-driven winds. Rapidly rotating stars suffer gravity darkening (von Zeipel 1924), producing cooler equatorial zones and hotter poles. Such stars also have higher escape speeds out the poles than at the equator, so the polar winds are faster. The oblate structure of the star produces a larger cross-section in the polar directions, and also the hotter poles produce much more radiative flux ($F_{\text{rad}} \propto T^4$). This is critical for a radiation-driven wind. This stronger radiative flux at the poles, combined with velocity-dependent forces, means that rapidly rotating stars have higher mass flux and higher wind speed out the poles (see Owocki et al. 1994, 1996, 1998; Owocki & Gayley 1997). This is for radiatively driven mass loss — different from the more intuitive case of mechanical mass loss from a spinning object, which should produce an equatorial flow (appropriate for RLOF).

Including a stronger polar wind for the present state of the central BSG would not change the qualitative picture in Figure 10, because a stronger wind out the poles would still escape unobstructed. It may, however, make it easier to produce this shape and to reconcile the required values of \dot{M} with those of normal BSG stars. Note that for a B1.5 lab star, the expected value of \dot{M} is $\sim 5 \times 10^{-7} M_{\odot} \text{ yr}^{-1}$, or perhaps a small factor less if we allow for clumping. This would be in rough agreement with our upper limit for SBW1 derived from IR observations, $\sim 3 \times 10^{-7} M_{\odot} \text{ yr}^{-1}$. However, for both SBW1 and SN 1987A, densities at the equator would seem to suggest a slightly lower value of \dot{M} , closer to $10^{-7} M_{\odot} \text{ yr}^{-1}$. Moreover, our assumed wind speed of 300 km s^{-1} (the same value assumed by Chevalier & Dwarkadas 1995) is somewhat lower than the speeds we expect for a B1.5 supergiant, closer to $500\text{--}600 \text{ km s}^{-1}$. Perhaps the factor of 2–3 discrepancy in \dot{M} and V_W is not too concerning, but allowing the central BSG to have a bipolar wind — with higher \dot{M} and V_W out the poles, and lower \dot{M} and V_W at low latitudes near the equator — would make the agreement better.

A bipolar wind from the BSG might also help explain another observed peculiarity of SN 1987A. Studies of the evolution of light echoes from SN 1987A have revealed a large bipolar shell, much larger than the triple-ring system seen in *HST* images (Sugerman et al. 2005; Crotts et al. 1995; Wampler et al. 1990). In the geometry advocated here, there are no polar caps in the inner nebula, so the strong BSG wind is free to escape out the poles to much larger radii. Doing so, a bipolar wind could sweep into the surrounding interstellar medium and create a much larger bipolar shell.

4.3 Origin of the Triple Rings Around SN 1987A

We have noted multiple times that while interacting-winds models can reproduce structures resembling the equatorial rings around SN 1987A and SBW1 by forming an hourglass shape (Blondin & Lundqvist 1993; Martin & Arnett 1995; Collins et al. 1999), the polar rings of SN 1987A have actually been an enduring problem with no satisfactory explanation. The nebula around SBW1 does not exhibit polar rings that are as prominent as those around SN 1987A, but the detailed geometry we see in SBW1 may provide some intriguing clues about how the polar rings might have been formed.

The key difference between previously published interacting-winds models and the model advocated here is the existence of a dense DPF off the compact and dense equatorial ring (Figure 10). We have argued that its existence in SBW1 is supported by the presence of dust interior to the thin H α ring (Figure 8), as well as the unusual kinematic structure of the emission lines in long-slit echelle spectra (Figure 11). Chevalier & Dwarkadas (1995) argued for the existence of a similar structure around SN 1987A based on the properties of the advancing blast wave. This DPF creates a stand-off shock front (reverse shock) in the equator at $R_{\text{RS}} = 0.05 \text{ pc}$, but at latitudes above and below the equator the interface will take a parabolic shape in cross section (Figure 10).

How does the existence of this DPF and reverse shock modify the situation? In this scenario, one would still expect the formation of a thin hourglass-shaped nebula as the H II region tries to expand into any neutral gas outside it (see Chevalier & Dwarkadas 1995). The fast BSG wind will escape in the polar direction and will sweep away any of this outer nebulosity, *but it will be prevented from doing so at low latitudes*. In effect, the DPF and reverse shock keep the BSG stellar wind at bay, and thereby shield the nebula at low latitudes. Therefore, we expect that the thin outer hourglass structure will remain at mid and low latitudes, as depicted in Figure 10.

Now, recall that the collision between the DPF and the BSG stellar wind leads to a nonradial flow of dense gas down the shock front (Figure 11). An interesting consequence of the proposed flow down the shock interface is that the densest gas will flow outward at a narrow range of latitudes above and below the equator. This flow may eventually intersect the hourglass structure, which in this picture is the outer boundary of the photoionised cavity — labeled as the ionisation shock front in Figure 10. Interestingly, the geometrical intersection of these two curved surfaces in three dimensions is a pair of plane-parallel rings above and below the equator. (This would still be true if the outer ionisation shock front were an hourglass, a sphere, or a cylinder.) If there is a density enhancement associated with this intersection, it may help explain the origin of the polar rings around SN 1987A and HD 168625.

Alternatively, a similar idea was suggested by Chiřă et al. (2008) based on their hydrodynamic simulations of a bipolar BSG wind interacting with a thin spherical shell formed by the terminal shock of the previous RSG phase. They assumed that as the star evolves in a blue loop after the RSG phase, the star must spin up, and that the wind from the BSG will have a bipolar shape for the reasons noted in §4.2.4. These authors showed that the collision of a bipolar wind with a thin shell could lead to a pair of polar rings. In this scenario, the existence of the reverse shock could help to stabilise the latitude range where the bipolar BSG wind and thin shell intersect, so that the rings would not be as transient as in those simulations.

We hope that the observations and discussion presented here will motivate new simulations that include the effects of a DPF. This basic picture also allows for some differences among objects, which may help explain some of the diversity in the structures seen around SN 1987A, SBW1, Sher 25, and HD 168625. For SBW1 and SN 1987A, we expect that the initial structures of the two nebulae were very similar,

but that in SN 1987A, the structure has been modified: the dense ring has become more fully ionised and the interior dust was probably vaporised by a UV flash from SN shock breakout. Even ignoring the supernova UV flash, however, certain aspects of the structure can be adjusted. For example, other central stars may have different values of Q_H or \dot{M} , either of which may change the relative location of the shock between the BSG and the photoevaporative flow, and may affect the opening angle. This could have important implications for understanding when the SN 1987A blast wave encountered the H II region (see Chevalier & Dwarkadas 1995; Gaensler et al. 2000). The stellar luminosity values for SBW1 and Sk-69°202 are very similar, so their mass-loss rates should be similar, but SBW1 is hotter (B1.5 instead of B3) and has a higher value of Q_H . This may strengthen the relative importance of the DPF somewhat in SBW1. Nevertheless, SBW1 and SN 1987A may trace one another more closely than in other BSG ring nebulae, such as Sher 25 and HD 168625, both of which have substantially higher stellar luminosities. Nevertheless, one could probably tune the basic picture presented here to be applicable to those two objects as well.

5 SUMMARY

In this paper, we have presented a series of multiwavelength images and spectra of the nebula around the blue supergiant SBW1, which is seen in the Carina nebula. The observations included the first images and spectra of this target obtained with *HST* using WFC3 and STIS, as well as IR images from *Spitzer* and Gemini South/T-ReCS. Analysis of this multiwavelength dataset has led to several conclusions about SBW1 and related systems, enumerated below.

(1) *HST*/WFC3-UVIS F656N and F658N images of SBW1 reveal a thin, clumpy ring, but do not show the long R-T fingers that have been invoked to explain the origin of the hot spots around SN 1987A when the tips of the R-T fingers are hit by the blast wave. Instead, the structure is more akin to beads along a string with little dense matter in between. Instead of arising when a wind swept into an extended thin equatorial disk, as suggested by hydrodynamical modeling of SN 1987A, the observed structure may suggest an episodic ejection of a ring that fragmented into clumps as it cooled.

(2) We noted that the episodic ejection of a slow, clumpy ring could result during a brief phase of RLOF, as seen in the RY Scuti eclipsing binary system. A previous RSG phase is not needed to explain the slow expansion speed of the ring.

(3) The radius of the ring, size and angular scale of clumps in the ring, and deviations from the average radius (wiggles) seen in SBW1 are all an excellent match to the structures seen in SN 1987A's ring.

(4) The radial velocity measured in our STIS spectra as well as the luminosity and extinction indicated by the SED both confirm the large distance of ~ 7 kpc (Smith et al. 2007), meaning that SBW1 is far behind the Carina Nebula and seen in projection, rather than actually being inside it.

(5) High-resolution images reveal complex diffuse emission filling the interior of the ring. H α emission seen by *HST* uniformly fills much of the ring interior, with two enhance-

ments in the H α flux about 1–2'' away from the star on both sides along the major axis. Much more importantly, mid-IR images obtained with Gemini South reveal strong dust continuum emission associated with these same positions. The warm dust emission residing inside the ring is critically important, because the dust cannot arise from the BSG wind.

(6) The IR SED reveals two distinct dust-temperature components: $T = 190$ K dust with a mass of only $10^{-5} M_{\odot}$, and ~ 85 K dust with a larger mass of $5 \times 10^{-3} M_{\odot}$. This implies a total gas mass for the SBW1 ring of at least $0.5 M_{\odot}$. High-resolution mid-IR images from Gemini South confirm that the cooler 85 K component arises from dust in the dense equatorial ring, whereas the warmer 190 K dust comes from the double-peaked diffuse emission in the ring's interior.

(7) Both H α and mid-IR images reveal a clear deficit of diffuse emission within 1–2'' of the central star, suggesting that a cavity has been cleared by the BSG wind.

(8) We propose a model for the origin of the observed structures in SBW1 that departs markedly from the standard interacting-winds model for SN 1987A. Instead of the equatorial ring arising as a consequence of a fast wind sweeping into a slow extended disk wind, we propose that the ring was ejected in an episodic event and then photoionised by the BSG. When the dense neutral clumps in the ring get ionised, they produce an ionised photoevaporative flow that has an important hydrodynamic effect because of the pressure of the ionised gas. The double-peaked diffuse H α and mid-IR emission inside the ring marks the location of a shock where the BSG wind collides with the dusty photoevaporative flow (DPF). This DPF structure is analogous to the "H II region" proposed by Chevalier & Dwarkadas (1995) to account for the expansion of the blast wave of SN 1987A.

(9) In this model, the DPF keeps the BSG wind at bay in the equatorial plane, thereby shielding the ring and other nebular structures at low latitudes. The BSG can expand out the poles unobstructed.

(10) When the DPF and BSG wind collide in the equator, they must flow downstream. The shock front probably takes on a curved shape, diverting the flow to a narrow range of mid-latitudes (see Figures 10 and 11).

(11) We note some implications for the origin of structures around SN 1987A. If the BSG wind expands freely out the poles (i.e., there are no polar caps in the nebula), it may help explain the existence of a much larger bipolar shell seen with light echoes (Sugerman et al. 2005). Moreover, the non-radial post-shock flow that is confined to a narrow range of latitudes (point 10 above) may help explain the existence of the polar rings around SN 1987A when this flow intersects the dense shell at the outer boundary of the H II region. We encourage further investigation of this idea using numerical simulations that account for the effects of a photoionised flow. As we note in the text, this photoionised flow is permitted to have an important dynamical effect because the initial expansion speed of the neutral dense ring is slow, comparable to the sound speed in the ionised gas.

ACKNOWLEDGMENTS

Support was provided by the National Aeronautics and Space Administration (NASA) through *HST* grants GO-11637, GO-11977, and AR-12623 from the Space Telescope Science Institute, which is operated by AURA, Inc., under NASA contract NAS5-26555. Additional support for this work was provided by

NASA through awards issued by JPL/Caltech as part of *Spitzer* programs GO-3420, GO-20452, and GO-30848. A.V.F. is also grateful for financial assistance from NSF grant AST-1211916. This publication makes use of data products from the Two Micron All-Sky Survey, which is a joint project of the University of Massachusetts and the Infrared Processing and Analysis Center/California Institute of Technology, funded by NASA and the National Science Foundation (NSF). We have also used data products from the Wide-field Infrared Survey Explorer, which is a joint project of the University of California, Los Angeles and the Jet Propulsion Laboratory/California Institute of Technology, funded by NASA.

REFERENCES

- Arnett W. D., 1987, *ApJ*, 319, 136
 Arnett W. D., 1989, *ApJ*, 343, 834
 Arnett W. D., Bahcall J. N., Kirshner R. P., Woosley S. E. 1989, *ARA&A*, 27, 629
 Bally J., Sutherland R. S., Devine D., Johnstone D. 1998, *AJ*, 116, 293
 Bertoldi F. 1989, *ApJ*, 346, 735
 Bertoldi F., McKee C. F. 1990, *ApJ*, 354, 529
 Blondin J. M., Lundqvist P. 1993, *ApJ*, 405, 337
 Bouchet P., et al. 2006, *ApJ*, 650, 212
 Brandner W., Chu Y. H., Eisenhauer F., Grebel E. K., Points S. D. 1997, *ApJ*, 489, L153
 Broos P. S., et al. 2011, *ApJS*, 194, 2
 Burrows C. J., et al. 1995, *ApJ*, 452, 680
 Chevalier R. A., Dwarkadas, V. 1995, *ApJ*, 452, L45
 Chiřă S. M., Langer N., van Marle A. J., Garca-Segura G., Heger A. 2008, *A&A*, 488, L37
 Collins T. J. B., Frank A., Bjorkman J., Livio M. 1999, *ApJ*, 512, 322
 Crotts A. P. S., Heathcote S. R. 2000, *ApJ*, 528, 426
 Crotts A. P. S., Kunkel W. E., Heathcote S. R. 1995, *ApJ*, 438, 724
 Draine B. T., Lee H. M. 1984, *ApJ*, 285, 89
 Fazio G., et al., 2004, *ApJS*, 154, 10
 Gaensler B. M., Manchester R. N., Stavelly-Smith L., Wheaton V., Tzioumis A. K. 2000, in *Asymmetrical Planetary Nebulae II: From Origins to Microstructures*, ed. J. Kastner, N. Soker, & S. Rappaport (San Francisco: ASP), 449
 Gehrz R. D., Smith N., Jones B., Puetter R., Yahil A. 2001, *ApJ*, 559, 395
 Gilman R. C. 1974, *ApJS*, 28, 397
 Grundstrom E. D., et al. 2007, *ApJ*, 667, 505
 Johnstone D., Hollenbach D., Bally J. 1998, *ApJ*, 499, 758
 Kochanek C. S. 2011, *ApJ*, 743, 43
 Leonard D. C., 2011, *Ap&SS*, 336, 117
 Luo D., McCray R. 1991, *ApJ*, 379, 659
 Martin C. L., Arnett W. D. 1995, *ApJ*, 447, 378
 Martins F., Schaerer D., Hillier D. J. 2005, *A&A*, 436, 1049
 Michael E., McCray R., Borkowski K. J., Pun C. S. J., Sonneborn G. 1998, *ApJ*, 492, L143
 Michael E., et al. 1999, *ApJ*, 509, L117
 Morris T., Podsiadlowski P. 2009, *MNRAS*, 399, 515
 Oort J. H., Spitzer L. 1955, *ApJ*, 121, 6
 Owocki S. P., Cranmer S. R., Blondin, J. M. 1994, *ApJ*, 424, 887
 Owocki S. P., Cranmer S. R., Gayley K. G. 1996, *ApJ*, 472, L115
 Owocki S. P., Gayley K. G. 1997, in *Luminous Blue Variables: Massive Stars in Transition*, ed. A. Nota & H. Lamers (San Francisco: ASP), 121
 Owocki S. P., Gayley K. G., Cranmer S. R. 1998, in *Boulder Munich II: Properties of Hot Luminous Stars*, ed. I.D. Howarth (San Francisco: ASP), 237
 Plait P. C., et al. 1995, *ApJ*, 439, 730
 Povich M. S., Smith N., Majewski S. R., et al. 2011, *ApJS*, 194, 14
 Price S. D. 1995, *Space Sci. Rev.*, 74, 81
 Puls J., Vink J. S., Najarro F. 2008, *A&A Rev.*, 16, 209
 Rieke G. H., et al. 2004, *ApJS*, 154, 25
 Shacham T., Shaviv N. J. 2012, preprint (arXiv:1206.6078)
 Skrutskie M. F., et al. 2006, *AJ*, 131, 1163
 Smartt S. J. 2009, *ARA&A*, 47, 63
 Smartt S. J., et al. 2002, *A&A*, 391, 979
 Smith N. 2006, *ApJ*, 644, 1151
 Smith N. 2007, *AJ*, 133, 1034
 Smith N., Bally J., Shuping R., Morris M., Kassis M. 2005, *AJ*, 130, 1763
 Smith N., Bally J., Walawender J. 2007, *AJ*, 134, 846
 Smith N., Bally J., Walborn N. R. 2010a, *MNRAS*, 405, 1153
 Smith N., Gehrz R. D. 2005, *AJ*, 129, 969
 Smith N., Gehrz R. D., Campbell R., Kassis M., Le Mignant D., Kuluhiwa K., Filippenko A. V. 2011, *MNRAS*, 418, 1959
 Smith N., Gehrz R. D., Humphreys R. M., Davidson K., Jones T. J., Krautter J. 1999, *AJ*, 118, 960
 Smith N., Gehrz R. D., Stahl O., Balick B., Kaufer A. 2002, *ApJ*, 578, 464
 Smith N., Povich M. S., Whitney B. A., et al. 2010b, *MNRAS*, 406, 952
 Smith N., Townsend R. H. D. 2007, *ApJ*, 666, 967
 Smith N., et al. 2003, *AJ*, 125, 1458
 Sonneborn G., et al. 1998, *ApJ*, 492, L139
 Sugerman B. E. K., Crotts A. P. S., Kunkel W. E., Heathcote S., Lawrence S. S. 2005, *ApJS*, 159, 60
 Sugerman B. E. K., Lawrence S. S., Crotts A. P. S., Bouchet P., Heathcote S. R. 2002, *ApJ*, 572, 209
 Townsley L. K., et al. 2011, *ApJS*, 194, 1
 Walborn N. R., et al. 1989, *A&A*, 219, 229
 Wampler E. J., Wang L., Baade D., Banse K., D'Odorico S., Gouffes C., Tarengi M. 1990, *ApJ*, 362, L13
 Wright A. E., Barlow M. J. 1979, *MNRAS*, 170, 41
 Wright E. L., et al. 2010, *AJ*, 140, 1868
 Zickgraf F. J., Humphreys R. M., Lamers H. J. G. L. M., Smolinski J., Wolf B., Stahl O. 1996, *A&A*, 315, 510